TEL AVIV UNIVERSITY
The Iby and Aladar Fleischman Faculty of Engineering
The Zandman-Slaner School of Graduate Studies

SUPER-RESOLUTION OF NEAR-INFRARED FLUORESCENT SINGLE-WALLED CARBON NANOTUBES

A thesis submitted toward the degree of
Master of Science in Biomedical Engineering

by
Barak Kagan

October 2022

TEL AVIV UNIVERSITY
The Iby and Aladar Fleischman Faculty of Engineering
The Zandman-Slaner School of Graduate Studies

SUPER-RESOLUTION OF NEAR-INFRARED FLUORESCENT SINGLE-WALLED CARBON NANOTUBES

A thesis submitted toward the degree of
Master of Science in Biomedical Engineering

by
Barak Kagan

This research was carried out in The Department of Biomedical Engineering
Under the supervision of Dr. Gili Bisker

October 2022

Acknowledgment

I would like to acknowledge my supervisor, Dr. Gili Bisker for her guidance, support throughout the process, and for preventing me from giving up in moments of crisis.

I would like to thank my lab colleagues - Dr. Adi Hendler-Neumark, Dr. Verena Wulf, Dr. Dotan Kamber and Roni Ehrlich for their patience, time and useful advices.

Thank you, Almog Friednlender and Ofer Haim for the uncompromising support around the clock, for the fascinating and relentless discourse on relevant issues, and for the comprehensive and friendly support in implementing the code.

Lastly, to Neta, for believing in me all the way through, and giving me the support to make it happen.

Abstract

Single-walled carbon nanotubes (SWCNTs) have unique optical, chemical, and physical properties, and are high aspect-ratio nanoparticles being 1-2 nm in diameter and up to several micrometers in length. SWCNTs can be utilized in numerous biomedical imaging and sensing applications, owing to their near-infrared (nIR) fluorescence between 900 – 1400 nm, which overlaps with the biological transparency window. However, in addition to their nanometric nature which is smaller than the common camera's resolution size (0.7-13 μm), their longer emission wavelengths compared to fluorescent emitters in the visible range result in a lower resolution due to the diffraction limit. Hence, super-resolution (SR) techniques which enhance our understanding of precise structural features and dynamic behaviors at the nano-scale, are necessary in order to fully exploit SWCNTs as optical probes for both spatial and temporal information and to fathom biological environments. Nonetheless, super-resolving fluorescence images of SWCNT in the nIR presents several challenges. First, SWCNTs are not point-emitters and can have turns, twists, and loops, impeding geometry-based SR techniques. Moreover, the SWCNT suspensions are heterogeneous in nature, having a wide length distribution and multiple chiralities, each of which fluoresce in a different wavelength. Finally, the longer wavelengths of the fluorescence, compared to common fluorophores in the visible range, further limits the resolution due to the diffraction barrier.

This work demonstrates the use of deep learning in general, and convolutional neural networks (CNNs) specifically, for achieving high-resolution images of SWCNTs in the nIR spectral range. Utilizing the advantages of state-of-the-art deep learning and CNNs we obtain high-resolution images for a variety of SWCNT densities and length

distributions, and a wide range of imaging conditions with challenging signal-to-noise ratios (SNRs). This essay shows, for the first time, a robust SR approach that requires no manual parameter tuning nor special equipment. Moreover, our approach does not require stochastic, blinking, or photo-switchable fluorophores, in contrast to other SR single-molecule localization microscopy methods such as stochastic optical reconstruction microscopy (STORM) or photoactivated localization microscopy (PALM).

We train an encoder-decoder architecture network, using super-resolution radial fluctuations (SRRF) analytical approach as our desired ground truth. We validate our CNN and show a notable improvement, on average, of 22% in the resolution and 47% in SNR compared to the original images for a broad range of SWCNTs shapes, lengths, and densities, whereas SRRF leads to only 24% SNR improvement. Further, we demonstrate real-time super-resolution of SWCNT videos without compromising the temporal resolution of the original sequence of frames. This work provides a significant milestone in the field of super-resolution (SR) microscopy using deep learning techniques to achieve an ultra-fast, parameter-free algorithm for super-resolving images of non-spherical emitters in the near-infrared at large, and of SWCNTs in particular, further advancing their applicability as optical probes at the nanoscale.

Publications

- Barak Kagan, Adi Hendler-Neumark, Verena Wulf, Dotan Kamber, Roni Ehrlich, Gili Bisker, *"***Super-resolution near-infrared fluorescence microscopy of single-walled carbon nanotubes using deep learning***", **Advanced Photonics Research**,* 3 (11), 2200244 (2022):

  Super-resolution methods are designed to overcome the diffraction limit and unravel nanometric structure dynamics. Kagan et. al. offer a fast, robust, parameter-free approach to yield super-resolved images of near-infrared fluorescent single-walled carbon nanotubes (SWCNTs), utilizing supervised deep learning and convolutional neural network, showing improved resolution for a variety of SWCNTs lengths and densities, and challenging imaging conditions.

- Roni Ehrlich, Verena Wulf, Adi Hendler-Neumark, Barak Kagan and Gili Bisker, "**Super-Resolution Radial Fluctuations (SRRF) nanoscopy in the near infrared**", ***Optics Express***, 30 (2), 1130 (2022):

  Super-resolution microscopy methods have been designed to overcome the physical barrier of the diffraction limit and push the resolution to nanometric scales. A recently developed super-resolution technique, super-resolution radial fluctuations (SRRF), has been shown to super resolve images taken with standard microscope setups without fluorophore localization. Herein, we implement SRRF on emitters in the near-infrared (nIR) range, single walled carbon nanotubes (SWCNTs), whose fluorescence emission overlaps with the biological transparency window. Our results open the path for super-resolving SWCNTs for biomedical imaging and sensing applications.

Table of Contents

List of Figures

List of Tables

1. Introduction

Single-walled carbon nanotubes (SWCNTs), visualized as a one-dimensional cylinder of a rolled-up sheet of carbon atoms arranged in a honeycomb lattice, find numerous biomedical applications including imaging and sensing in the nIR.[1,2,11,3–10] For sensing, functionalized SWCNTs can bind specific analytes such as proteins, small molecules, metal-ions, or bacteria, and exhibit fluorescence modulations upon interaction, whereas for imaging, they can be easily tracked in complex biological environment owing to their near Infra-Red (nIR) fluorescence in the range of 900-1600 nm.[12,13,22–24,14–21]

In order to fully exploit SWCNTs as optical probes for both spatial and temporal information, the nanotubes should be individually imaged, tracked, and resolved.[25–28] By doing so we can bridge the gap between cellular observations and molecular structure knowledge.

However, the diffraction of the long nIR wavelengths SWCNTs emits limits the resolution, creating an additional challenge compared to the visible range, when attempting to observe internal structures. Specifically, SWCNTs fluorescence emission occurs primarily between 900–1600 nm[29] resulting in a diffraction limit of ~450-800 nm whereas for commonly used dyes the resolution limit is in the range of 250-300 nm.[30]

Therefore, there is a growing need for improving the spatial resolution of fluorescence images of SWCNTs in the nIR in order to fully utilize their optical properties and fluorescence emission in the biological transparency window for imaging, tracking, and sensing.[19,20,31] Nonetheless, most of nowadays super-resolution microscopy techniques are depended on specific imaging equipment, long processing time, or can resolve only geometrically-homogeneous sensors.

In this thesis, I have developed a machine learning algorithmic approach for super-resolution of SWCNTs in the nIR range. I have demonstrated my approach on nIR fluorescence images of SWCNT samples with various length distributions and densities (hence, proving it to be independent on the markers geometrical-homogeneity), as well as complex image conditions [e.g., bright background with low signal to noise ratio (SNR), and closely located SWCNT with overlapping point-spread functions (PSFs)] and real-time movies of diffusing SWCNTs, and showed an average full-width-half-max (FWHM) improvement of 22.4% compared to the original LR images.[32] To do so, I first synthesized heterogeneous samples of short and long nanotubes by tuning sonication times (Figure 1a), and imaged immobilized SWCNTs in total internal reflection fluorescence (TIRF) mode to optimize the SNR (Figure 1b). Then, I addressed the aforementioned challenge of the diffraction limit in the nIR range, and counter the need for an ultrafast, parameter-free algorithm for precise localization and super-resolution of SWCNT images by harnessing the advantages of a convolutional neural network (CNN) (Figure 1c). Utilizing basic augmentation operators, I expanded the data set of TIRF low-resolution (LR) images by a factor of almost 10, from which I obtained a labeled data set of high-resolution (HR) images, by implementing an existing super-resolution algorithm, as our ground truth (GT) HR images. The LR and HR data sets are used as a part of the supervised learning process of the CNN. My results extend the applicability of SWCNTs as optical probes for imaging in complex and heterogeneous biological samples, and open new avenues for super-resolution microscopy in the near-infrared range.

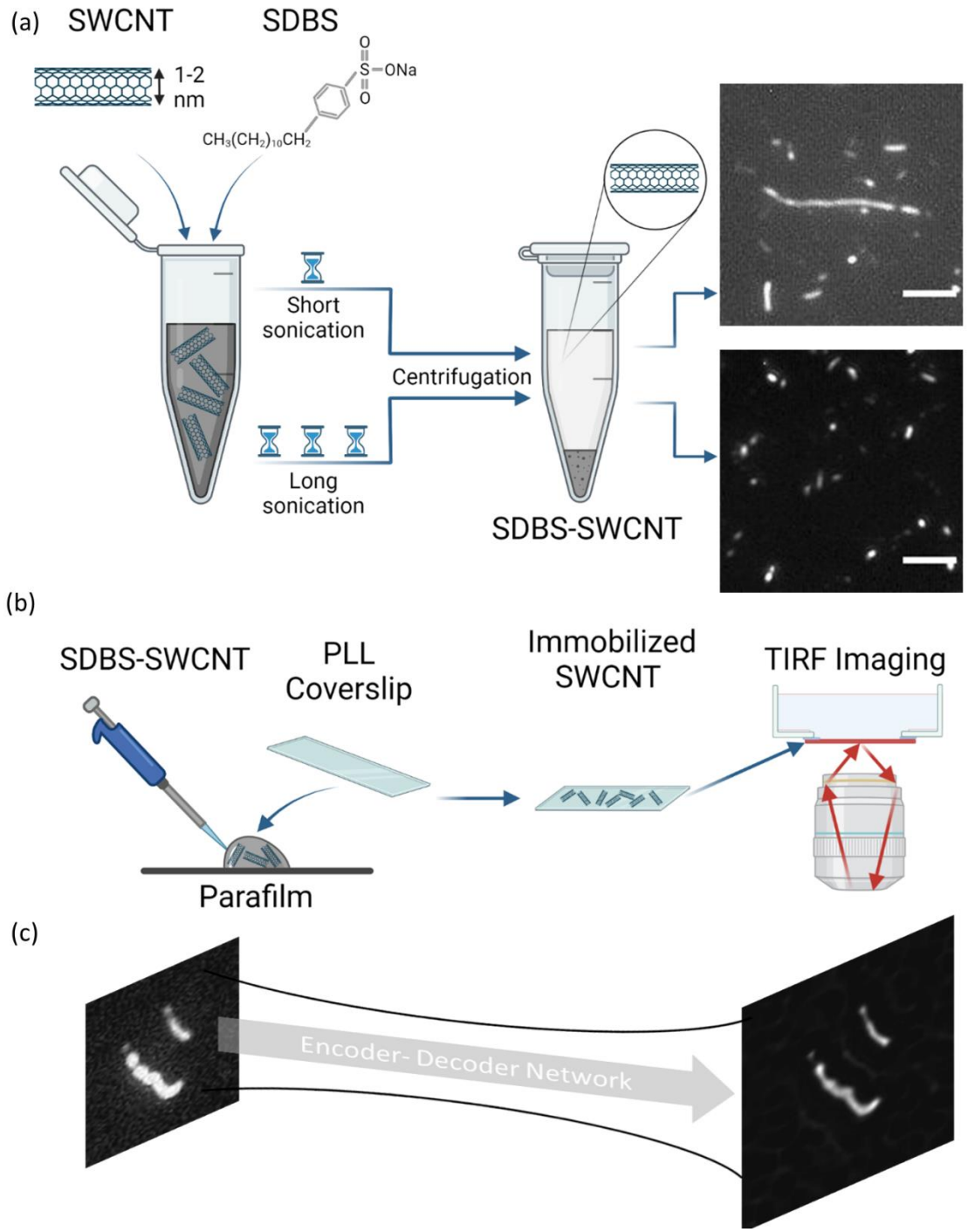

Figure 1. Schematic representation of the working protocol. a) SWCNTs suspension with SDBS using varying sonication times for producing different length distributions of nanotubes, with representative fluorescent images of SWCNTs lengths. Scale bar stands for 5 μm. b) SWCNT immobilization on poly-L-lysine-coverslip for TIRF imaging in the nIR wavelength range. c) Encoder-decoder convolutional neural network (CNN) representation for high-resolution images of SWCNTs. Created with BioRender.com.

2. Theoretical background

2.1. Single walled-carbon nanotubes

2.1.1. Structure and properties

Carbon nanotubes are rolled up cylinders of graphene sheets (Figure 2a) composed of sp2- hybridized carbon atoms.[1,20] With an inner diameter of 1-2 nanometers, and length of 300 nm – 10 μm,[1,29,33] SWCNTs have unique physical,[34,35] chemical,[36,37] mechanical,[38] and electronic properties.[39] Both the SWCNT's chemical and physical properties are structure-dependent, as there are many different angle to roll-up the SWCNTs which leads to a variety of SWCNTs structures. The angle values can be described using two integer values (Figure 2b) – a_1 and a_2, which denotes the lattice basic vectors of the graphene layer. Hence the SWCNT's angle at which it can be rolled up can be described by a vector which is a linear combination of the two:

$$c = na_1 + ma_2 \quad (1)$$

The different geometries are described by the (n,m) index and are known as the SWCNTs chirality. The (n,m) index is related to diameter of the SWCNT:

$$d = \frac{|c|}{\pi} = \frac{a_0}{\pi}\sqrt{n^2 + nm + m^2} \quad (2)$$

Where a_0 is the graphene lattice constant (0.246 nm).

The (n,m) values also describe whether SWCNTs exhibit metallic, semimetallic or semiconducting properties. The density of electronic states, as well as the band gap between the conduction and valence band are related to these properties and determine whether a SWCNT is fluorescent.[1] Due to the electronic band-gap between valence and conduction band semiconducting SWCNTs are fluorescent in the nIR.[40] Transitions from the conduction to the valence band lead to fluorescence, where the E_{22} transitions lead to absorption (v2 → c2) and the E_{11} transition to the fluorescence emission (c1 → v1) (Figure 2c)[40]

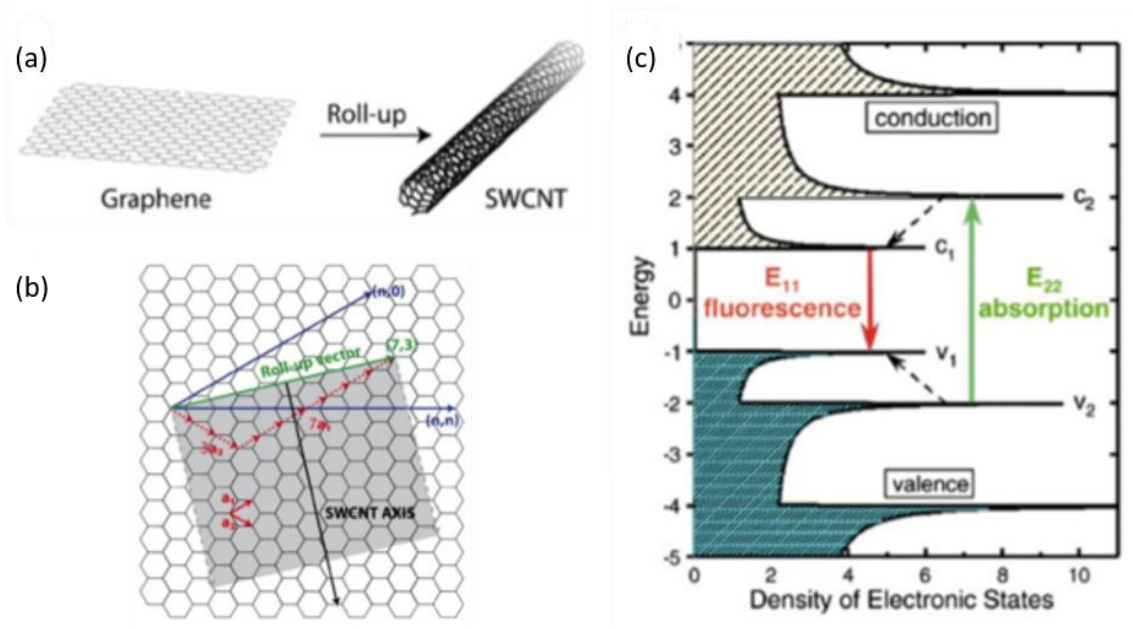

Figure 2. SWCNT's structural properties. a) Illustration of SWCNTs consist of a graphene sheet rolled up to form a cylinder. b) The roll up vector c is defined as $c = na_1 + ma_2$. SWCNT are generated by rolling up the graphene sheet along this vector and superimposing the first and the last carbon atom. An example (green) for the (7, 3) SWCNT is given where $c = 7a_1 + 3a_2$. c) Density of electronic states of a semiconducting SWCNT.

Unfunctionalized SWCNTs consider to be hydrophobic[20] and tend to form bundles due to strong van der Waals forces. Functionalizing SWCNTs with amphiphilic molecules or polymers, which is possible owing to the material's high surface area,[29] can form a colloidal suspension of individually dispersed SWCNTs.[29,41]

2.1.2. SWCNTs as imaging probes

The unique optical and electronic properties of SWCNTs make them favorable as fluorescent sensors for biomedical applications, in particular due to the SWCNTs fluorescence emission in the nIR range (900-1600 nm) which does not photobleach nor blink.[30,42,43] Generally, when super resolving structures within biological tissue, imaging in the nIR with an emission wavelength of λ>900 nm, is favorable due to the "optical transparency window" where light scattering is suppressed, and imaging penetration depth is maximized.[44,45] Moreover, given proper functionalization SWCNTs are highly

bio-compatible,[46,47] making them biocompatible probes in the biological transparency window range, where commonly imaging relies on nanoparticle probes containing toxic elements.[48,49] As so, SWCNTs have already were successfully utilized as imaging and sensing probes in various applications such as within plants,[10,50–52] live cells,[53–57] whole animals,[19,42,58–60] and brain tissue,[61,62] for example the brain extracellular space (ECS).[63] Beside than extracting information on a biological environment, imaging and monitoring moving SWCNTs in fluids[12,13] or gels[14] as well as fixed samples[15–18] can be beneficial for applied science and for our understanding of SWCNTs dynamics.

Yet, imaging the SWCNTs fluorescence in the nIR gives rise to a major challenge as the longer emission wavelengths > 900 nm, result in a lower resolution due to the diffraction limit, compared to imaging with shorter emission wavelengths in the visible range using common fluorescence dyes,[30] compromising the resolution of the taken image. Another challenge attached to SWCNT imaging, is the heterogeneity of SWCNT samples both in their shape-geometry, stemming from synthesis and suspension procedures which result in a wide distribution of SWCNTs lengths,[64–66] and in emission wavelengths, originate from the material properties. Those heterogeneous properties hinder the ability to individually resolve SWCNTs as imaging probes using both standard imaging methods or super-resolution techniques alike.

2.2. Super-resolution microscopy methods

Fluorescence microscopy is a widely-applied and invaluable tool for monitoring sub-cellular biological processes in real-time,[67–69] yet its spatial resolution is limited, according to Abbe's diffraction theory,[70,71] by approximately half the wavelength of light. Imaging in the nIR range with longer wavelengths than the visible light further exacerbates this issue. Still, favorable for biomedical imaging, the nIR range overlaps

with the biological transparency window,[72–74] enabling numerous biomedical applications such as sensing and imaging within deep tissue and cell-culture samples with minimal auto-fluorescence, absorption, and scattering interferences.[44,45,75] In standard fluorescence microscopy, both the quality and resolution of the images are predominantly limited by the optics, the photophysics of molecular emitters, and the sensor technology, posing a challenge for obtaining high-resolution images. Utilizing image reconstruction methodologies in fluorescence microscopy to solve deconvolution or super-resolution problems can improve the resolution, and also offer solutions to additional problems such as image denoising, registration, stitching, and fusion.[76–78] In deconvolution, for instance, a precise understanding of the optical system's properties (e.g. the PSF or the system's numerical aperture) and the characterization of the accompanying noise are required. Such classical methodologies have led, among others, to the design of popular algorithms such as Richardson–Lucy deconvolution,[79,80] which requires knowledge of the PSF of the microscope and assumes Poisson noise statistics. Without such prior knowledge, data-driven or data-based methods may be more broadly applicable to solve image reconstruction problems.[81] Super-resolution algorithms achieve their goal by localizing a sparse set of emitting fluorophores in single or multiple frames, through stochastic, analytical, or mathematical approaches. Some super-resolution methods are considered localization algorithms that provide a table of localized positions of the emitters, whereas other methods provide a super-resolved image without localization.[82,83] In the past years, many super-resolution microscopy methods have been developed[28] to overcome the diffraction limit and to enable observations of features at a nanometric scale[84] by utilizing photo-controlled emission of fluorescent molecules.[85] Camera-based super-resolution approaches[86] such as single-molecule localization microscopy (SMLM)[84] methods, namely, photo-activated localization microscopy (PALM),[87,88] stochastic

optical reconstruction microscopy (STORM),[89,90] and points accumulation for imaging in nanoscale topography (PAINT),[91] rely on acquiring a sequence of diffraction-limited images of a sparse set of blinking fluorophores by either molecular collisions or local chemical environment. By localizing the emitting fluorophores with high precision based on their PSFs frame-wise, and combining the emitter positions from all the frames, a single super-resolved image is procured. A similar SMLM strategy was demonstrated using SWCNTs functionalized with photo-switchable molecules, such that ultraviolet (UV) light illumination resulted in blinking of the SWCNT fluorescence by modulating the charge transfer to the nanotubes.[92] In these approaches standard equipment such as a wide-field microscope, a sensitive camera and continuous-wave lasers for excitation and activation are used,[93] however, a set of frames and a stochastically blinking fluorophores are necessary to achieve one single HR image.

In contrast, illumination pattern-based approaches which do not rely on the use of specific blinking emitters, grant the ability to extract nanoscale structures by mathematical reconstruction as a second stage for frequency shifted illumination[94,95]. Yet, those methods, such as structured illumination microscopy (SIM),[95] stimulated emission depletion (STED)[96] and reversible saturable/switchable optical linear fluorescence transitions (RESOLFT),[97] may often require specialized optical components.[86] Analytical super-resolution microscopy methods on the other hand, offer an instrumental simplicity, such as super-resolution optical fluctuation imaging (SOFI),[98] and super-resolution radial fluctuation (SRRF).[86,99]

Super-resolution microscopy push the boundaries of resolving nanometric structures and dynamics, and can shed light on complex biological structures in the microscale utilizing imaging probes[100] and single particle tracking (SPT).[14,101] This method, (i.e., SPT) which has been used to unfold dynamic information in many systems such as crystalline

hosts,[102] catalytic conversions,[103] and heterogeneous biological architectures,[26,27,104,105] is achieved by resolving frame by frame video recordings of single-particle diffusion to reconstruct the particle trajectory.[106,107] A notable advantage of SWCNTs is that they can be used to generate HR data of various complex environments in the nIR range, rendering them favorable imaging probes for HR bio-imaging.[28]

2.3. Super-resolution radial fluctuations

Super-resolution radial fluctuation (SRRF), is a recent developed analytical approach for super-resolution microscopy, that eliminates the need for specialized optical components, or fluorophore detection and localization,[86] and can be performed on standard wide field or TIRF microscope[86] imaging setups.

For a given sequence of images SRRF magnifies each pixel into subpixels, and calculates a "radiality" value based on the local symmetry resulting from the microscope PSF, yielding a "radiality stack".[99] For each subpixel the radiality value relates to the probability of it containing the center of a fluorophore.[86,99] Temporal correlations within the radiality stack are then used to create the final SRRF image.[86,99] The radiality stack created by SRRF preserves information in the gradient field which would be discarded by other localization techniques.[86] As such the radiality map on its own can already improve the resolution prior to the temporal analysis as we have demonstrated by applying SRRF to a single frame of a SWCNT in prior research done in our lab.[108] SRRF has been used for imaging cellular processes,[99,109–117] distinguishing DNA base-pair distance,[12] calcium imaging,[118] ultrasound microvascular imaging,[119] and traction force microscopy,[120] proving to be highly successful and widely used. Recently, SRRF has been usefully applied to nIR fluorescence images and videos of SWCNTs.[108]

2.4. Convolutional neural networks

Another highly promising paradigm in the field of image processing and computer vision in recent years is machine learning,[121–125] with CNNs[121,126–133] spearheading the advancements, showing impressive results in a variety of applications such as single-image resolution enhancement[134–137] and segmentation.[138,139]

CNN consists of input and output layers, as well as several hidden layers. The hidden part of CNN consists of a convolutional layer (i.e. 2 or 3-dimentional convolution is performed on the input data matrix using a moving kernel), pooling layer, and a fully connected classifier, which is a perceptron that processes the features obtained on the previous layers. Consider the part of CNN, which is responsible for the selection of features, and consists of a spatial convolution layer and a pooling layer that implements the max pooling operation.[140] Suppose that the image I consisting of R rows, C columns and D color channels is the input of CNN (e.g. RGB images have a $D = 3$ while greyscale images have $D = 1$). The CNN input can be described as a three-dimensional function $I(x, y, z)$ in this case, where $0 \leq x < R$, $0 \leq y < C$ and $0 \leq z < D$ are the spatial coordinates, and the amplitude I at any point with coordinates (x, y, z) is the intensity of the pixels at that point. Procedure for obtaining characteristics in arrays convolutional layer can be represented as

$$I_f(x, y) = b + \sum_{i=-t}^{t} \sum_{j=-t}^{t} \sum_{k=0}^{D-1} W_{i,j,k} \cdot I(x + i, y + j, k) \quad (3)$$

Where: I_f is the predicted matrix (feature map), $W_{i,j,k}$ is a $w \times w \times D$ kernel for processing D 2-dimentional arrays, b is an offset parameter[141] and $t = \frac{w-1}{2}$. CNN usually uses a large number of filters in the convolutional layer which leads to a sharp increase

in the amount of data processed in the network. The pooling layer of max pooling in some considered neighborhood is used to reduce them.[142] Figure 3 schematically shows a convolutional process of yielding a feature map and a max pooling operation using a filter mask of size $w \times w$ and stride w.

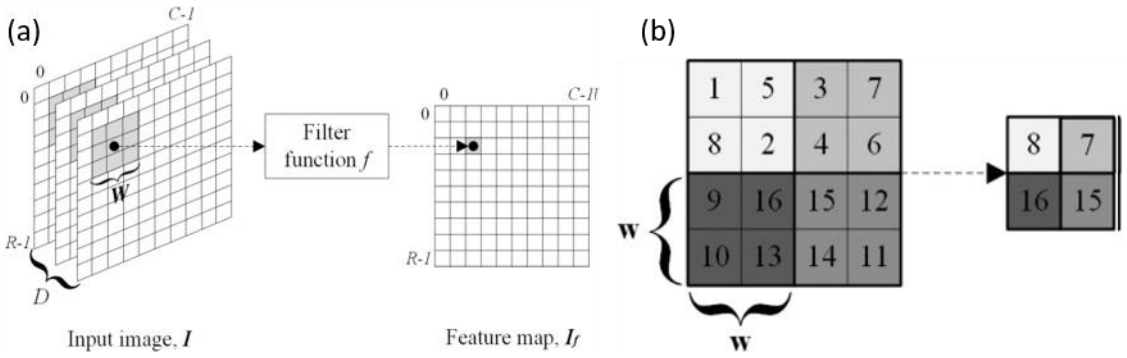

Figure 3. Representative principles of CNN layers. a) Represention of obtainment of feature maps post-convolutional layer. b) Max-pooling layer principle representation.

However, the CNN in this work lacks the fully connected classifier as the goal-output is a new image matrix, therefore a fully-convolutional-network (FCN) design was embraced. The most widely employed CNNs architectures for image segmentation are variants of so-called ‘‘encoder–decoder networks’’ proposed initially for unsupervised feature learning.[143] These encoder–decoder networks can obtain lower-level spatial resolution features together with a deep perception of the image (semantic recognition) via down-sampling.[144] They can also obtain higher-level spatial resolution features for highly accurate recovery of the image via upsampling which is in favor of a key assumption in super resolving images that states that high-frequency data is redundant as it can be accurately reconstructed from low frequency components. The general semantic segmentation task is to partition an image into a set of coherent regions that are connected and non-overlapping, and that enable homogeneous pixels to be clustered together.[145] A FCN is an end-to-end image segmentation method[138] modified through replacing the fully connected layer in a classification network by a transposed convolutional-layer[144]

but can easily transform its task to super-resolving images due to the similarity in pre-mentioned assumptions and capabilities of the FCN.

CNN-based approaches benefit from short computation times and do not require sample-dependent parameter tuning, in contrast to other super-resolution analytical methods, and hence can be used as a robust super-resolution methodology for real-time measurements under different samples properties.

3. Research objectives

As explained in the introduction, this work aims to embed the use of deep learning techniques for super-resolution method on individually dispersed SWCNTs imaged using a microscope setup with TIRF-illumination in the nIR range, and to offer an accessible, user-friendly, super-resolution algorithm.

First and foremost, the main motivation for this work is to enable a more accurate sub-diffraction spatiotemporal visualization of SWCNT, in order to advance the understanding of SWCNT's performances under various biological environments, and thus eventually to support various developments of SWCNTs as sensing and imaging probes. Nonetheless, the motivations behind implementing specifically a deep-learning based super-resolution algorithm in the nIR can be separated into two main aspects: the imaged materiel aspect, and method's restrictions aspect.

On the one hand, the growing potential of SWCNT to act as a bio-sensor increasing the need for super resolving images taken within complex biological samples in order to enhance the understanding of SWCNT's dynamics in different environments. Yet, minor changes in the imaging setup or the imaged sample can lead to a wide variety of complex imaging condition and the imaged SWCNT's properties. Therefore, the first goal was to develop a robust technique to resolve diverse lengths, densities and shapes (circular dots, short straight lines and long curvy lines) of the SWCNT suspensions.

Next milestone was to tackle the limitations of nowadays super-resolution methods. As explained in the theoretical background chapter, all existing algorithms would either require a set of multiple images to yield one resolved frame (impairing temporal resolution), a sample-dependent parameter tuning, specialized illumination imaging setup, or would take up long processing time. Accordingly, by utilizing deep-learning virtues

we aimed our method to address these challenges by eliminating the need for special imaging components, establishing a parameter-free method, and offering a real time algorithm for single frames.

We believe that with its simplicity and robustness, our network will aid in paving the path to sub-diffraction super-resolved images in the nIR, offering a better understanding of SWCNT-based structures at the nanoscale level and help in designing biocompatible sensors.

4. Methods

4.1. SWCNT suspension

1 mg mL^{-1} HiPCO Single-walled carbon nanotubes (SWCNTs, Nanolntegris) was suspended in 4 wt% sodium dodecylbenzene sulfonate (SDBS) (Sigma-Aldrich), by a direct tip sonication (8W for 5-20 seconds, QSonica Q125). Different sonication times were applied to yield varying SWCNT lengths (Figure 1a). Afterwards, the suspension was centrifuged twice (90 minutes, 16100 RCF, 25°C, Eppendorf) to separate individually suspended SWCNT from aggregates and impurities. The top 80% of the supernatant was extracted after each centrifugation step and the pellet discarded.

4.2. SDBS-SWCNT characterization

The absorption spectrum of the SDBS-SWCNT suspension was measured using an ultraviolet-visible-nIR (UV-Vis-nIR) spectrophotometer (Shimadzu UV-3600 PLUS). The excitation-emission map of the SDBS-SWCNT suspension acquired with the use of a nIR microscope coupled to an InGaAs detector, utilizing a spectrograph (PyLoN-IR 1024-1.7 and HRS-300SS, Princeton Instruments, Teledyne Technologies). A super-

continuum white-light laser (NKT-photonics, Super-K Extreme) coupled to a tunable bandpass filter (NKT-photonics, Super-K varia, $\Delta\lambda = 20$ nm) was used for excitation.

4.3. SWCNT immobilization

Microscope coverslips of 18 mm in diameter were immersed in 0.1% poly-L-lysine (PLL, Sigma-Aldrich) solution for 5 minutes, and rinsed with ethanol and water. 150 µl of 0.8 mg L^{-1} SDBS-SWCNT suspension was dropped on a laboratory film (Parafilm, Bemis, USA), on top of which the PLL-coverslip was placed for 5 minutes and rinsed again with water only. Subsequently, the PLL-coverslips with the immobilized SWCNTs were sealed using standard nail polish and placed on top of an imaging glass slide (Figure 1b).

4.4. nIR fluorescence imaging

Total internal reflection fluorescence (TIRF) microscopy imaging was done using an inverted fluorescence microscope (Olympus IX83) with a 100X TIRF objective (Olympus UAPON 100XOTIRF). SWCNT suspensions were excited by a 730 nm CW laser (MDL-MD-730-1.5W, Changchun New Industries) through a 900 nm long-pass dichroic mirror (Chroma, ET900lp). The near-infrared fluorescence emission was detected after a 900 nm long-pass emission filter (Chroma, ET900lp) using an InGaAs-camera (Raptor, Ninox 640 VIS-nIR) with a digital gain of 6 dB. For immobilized SWCNTs at varying densities, 100 frames were acquired in TIRF mode at 10 frames per second (fps) frame rate and 80-100 msec exposure time. In order to verify the network robustness to images with a variety of background intensities and SNRs, multiple neutral density (ND) filters were used in the range of ND02-ND10. All images (total of 129) were of size 640×512 pixels.

4.5. Visible-wavelength range fluorescence imaging

Visible-wavelength range fluorescence images were taken with the same setup as used for the nIR imaging, with one modification of the dichroic mirror that directs the fluorescence emission light to the relevant camera, an EMCCD in this case. The same microscope and objective were used. Likewise, SWCNT suspensions were excited by a 730 nm CW laser (MDL-MD-730-1.5W, Changchun New Industries). To detect the SWCNTs fluorescence emission using the EMCCD camera (Andor, iXon Ultra 888), the 900 nm long-pass dichroic mirror, used to reflect the >900 nm emission to the nIR camera and <900 nm to the visible camera, was replaced with an 1100 nm long-pass dichroic mirror (Chroma, CT1100LPXRXT), directing the emitted light up to 1100 nm to the visible EMCCD camera. The images were taken with an exposure time of 100 msec and a digital gain of 1 dB. The same sample was imaged in both cameras (visible and nIR) by switching the 900 nm and 1100 nm long-pass dichroic mirrors. The EMCCD images of size 1024×1024 were first aligned with their corresponding images taken with the nIR camera using MATLAB 2020a.[146] The aligned imaged of the EMCCD and InGaAs cameras, 742×594 pixels in size, were then cropped to cubic 512×512 size images and could be overlaid (Figure 4).

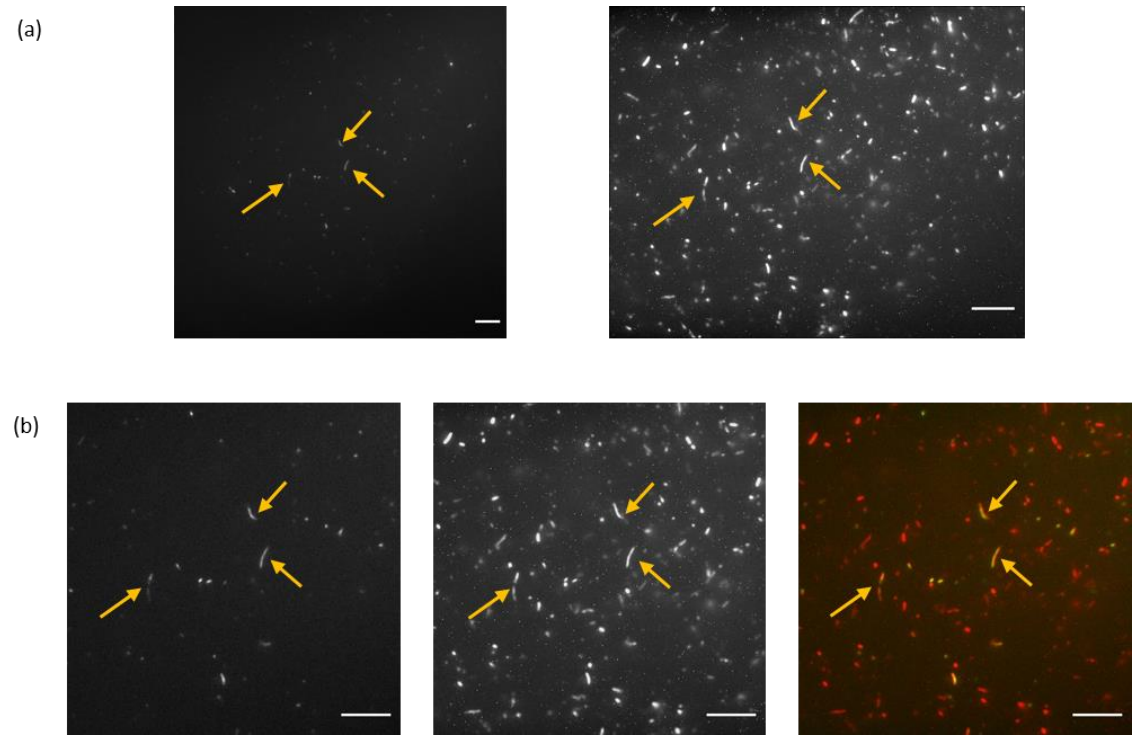

Figure 4. Andor (visible range) and Raptor (nIR range) image registration. a) From left to right: initial Andor camera image (1024×1024 pixels), and its corresponding Raptor camera image (640×512 pixels). b) From left to right: correlated and cropped Andor camera image (512×512 pixels), its corresponding correlated and cropped Raptor camera image (512×512 pixels) and an overlay image of both. Scale bar stands for 10 μm in all images. Yellow arrows indicated corresponding SWCNTs in both cameras.

4.6. SRRF analysis

Initial preprocessing of the images included a single pixel radius median filter to de-speckle the images, and a rolling ball algorithm (radius 50) to remove the background using ImageJ.[147][86] Then, high-resolution images were obtained using a Super-Resolution radial Fluctuations (SRRF) algorithm[86,108,117] using a ring radius of 0.5, radiality magnification of 4, and 6 axes in the ring. SRRF temporal analysis was done using a temporal radiality average (TRA), and an intensity weighting was preformed to enhanced radiality peaks.[86] Since the SRRF output images were used as the data labels, background removal (radius 50) and contrast enhancement (various factor of 0.01-0.1%)

were applied in ImageJ[147][86] to improve the images quality (See Figure 5a for visual representation). The background removal and contrast enhancement were preformed manually on each SRRF image to achieve the best quality output considering the input image properties such as SWCNTs density, image brightness, and number of frames, which directly affected the SRRF results. The preparation process of the labeled data is described in Figure 5a.

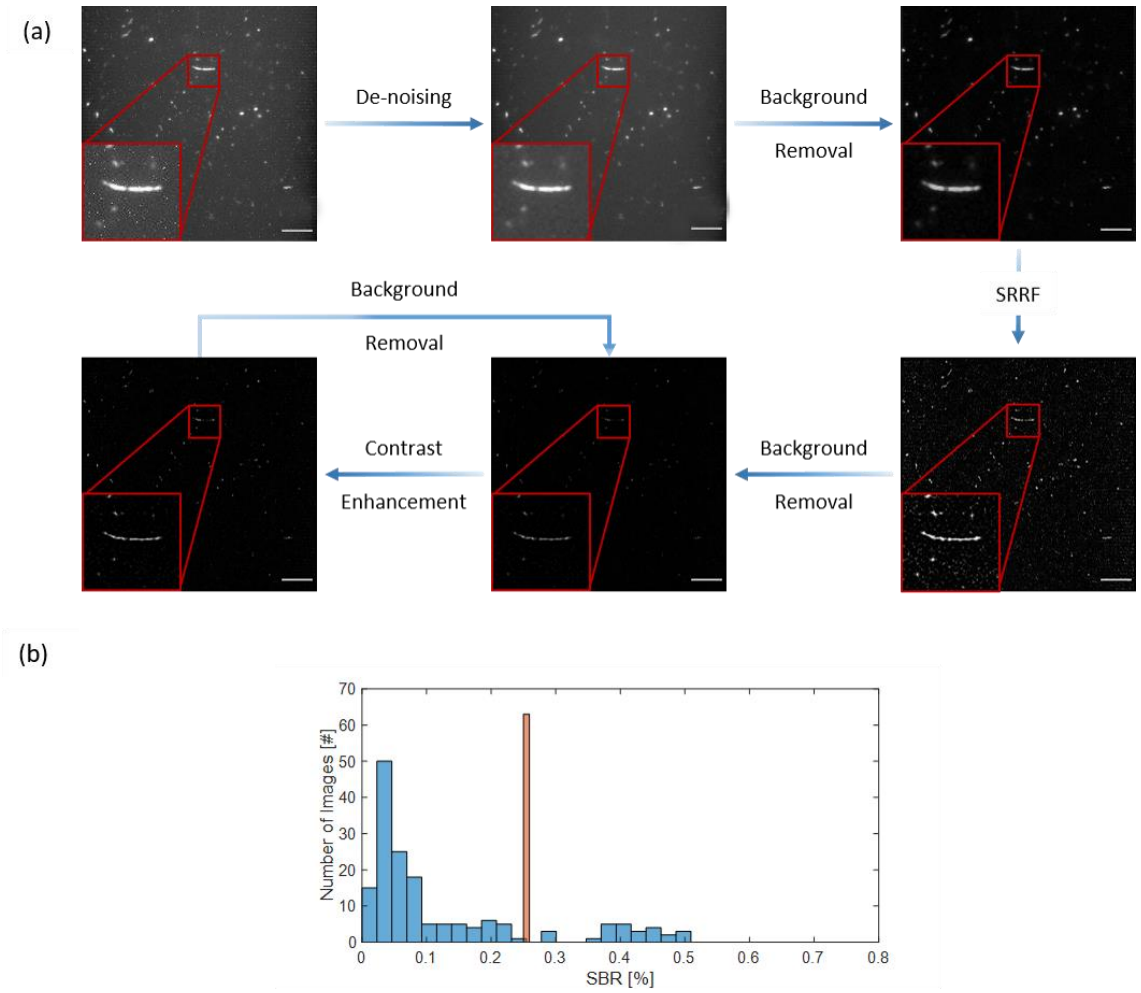

Figure 5. Original data set preparation. a) Preparation of the HR labels. All images went through the same steps of de-noising, background removal, and SRRF algorithm, then manually tuned using background removal and contrast enhancement to yield optimal results. Scale bar is 10 µm. b) Image classification according to densities using histogram thresholding over summed pixel value of binary images.

4.7. Images density classification

Following the formation of the initial data sets, the images were classified by their SWCNTs visible density. At first, the images went through binarization (i.e., notable SWCNT were labeled as 1, background as 0), using a grey-scale threshold value that was calculated using Otsu's method[148] and was iteratively and manually tuned to produce optimally binarized images. Subsequently, the number of pixels per image was summed, and using the Otsu's method, a separation threshold was extracted and constituted the pixel sum threshold representing the image density (Figure 5b). Threshold was set to be an SBR value of 0.257% (marked in orange in Figure 5b). All images with summed pixels value lower than the threshold were categorized as low-density images, whereas the rest were categorized as high-density images. Final data set sizes are described in Table 1. Out of the total 129 images, 108 were classified as low-density images and the rest as high density, resulting in an initial density ratio of 0.19. Images density classification was performed on the SRRF HR output images considering their better contrast, as it simplified the threshold finding process. The same predicted classification was assigned to the labeled image as well as the corresponding LR raw image.

Table 1. Data set sizes of the different densities

Data set	Low density	High Density	Total
Initial pre-augmentation	108	21	129
Post-augmentation	944	248	1,192
Training	869	223	1,092
Validation	75	25	100
Test	17	5	22

4.8. Data augmentation

Since different cameras produce images with different resolutions and aspect ratios, we chose a square size of 512×512 pixels as the input image dimensions. One advantage of this self-imposed restriction is the ability to utilize each raw image more than once by cropping different portions to yield a square image, thus augmenting our dataset. Raw images that contained a considerable number of SWCNTs in the lateral regions of the frame were cropped twice, once for the left side square and once for the right side. On the other hand, images with sparse information, mostly centered, were cropped only once to maximize the number of SWCNTs in the cropped frame. This method increased our data set by a factor of 1.1-1.2 to a total amount of 149 images. After manual cropping according to the spatial data distribution in each image, all of the images were augmented by using 90 degrees rotations and a horizontal flip (Figure 6), increasing our data set by a factor of 8. By doing so, we managed to increase our 129 initial images to a final data set to 1192 images, with a density ratio of 0.26 of high vs low densities. Eventually, out of the final training dataset of 1192 images, 1092 (91.6%) images were used strictly for training, whereas the remaining 100 (8.4%) images were used for validation (Table 1). Network performances were tested on a new test data set of 22 new images with various SWCNTs densities and lengths, which were not included in the initial training and validation database. All augmentation methods were applied on both the raw and labeled images, implemented with MATLAB 2020a.[146]

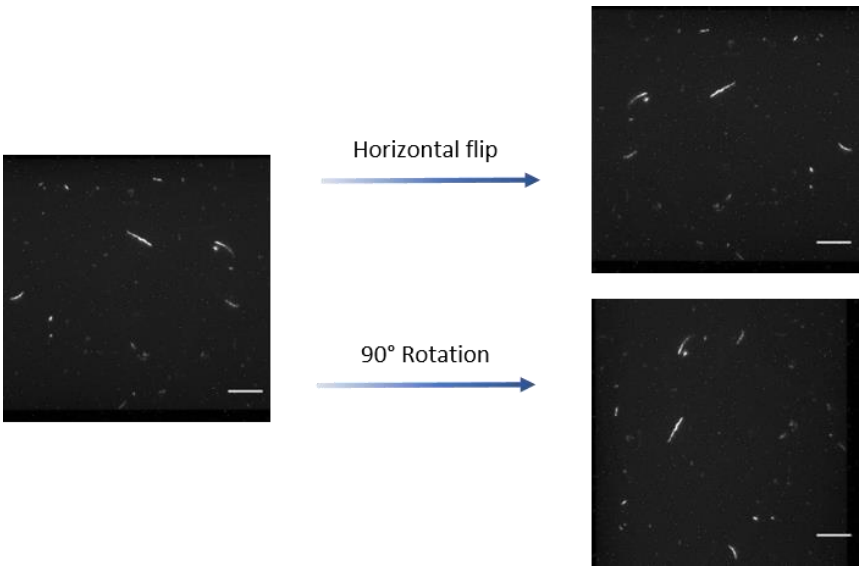

Figure 6. Image augmentation for enlarging the data set. Scale bar is 10 µm.

4.9. Data-sets preparation

The post augmentation data set consisted of 1192 matching pairs of LR and SRRF-HR grey scaled images. The final data set was divided to train and validation sets with the ratio of 9:1 respectively. Through this separation, the 0.26 ratio between high to low density images was maintained (Figure 5b). All pixel values of the input images were normalized to the range between 0 to 1. Network performances were tested on a test data set of 22 images with various SWCNTs densities and lengths.

4.10. Architecture and loss

Inspired by previous works such as Deep-STORM super-resolution-microscopy network[83] and based on U-NET encoding-decoding structure,[138,139] our network first encodes the spatial representation of the image features, through a monotonic logarithmic-scale decrease in image size and an increasing depth, and then decodes the same data by a reverse expansion section (Figure 7). The network first goes through 4 encoding blocks of the same structure – a 2D-convolution with 3×3 filter applied, followed by a non-linear ReLu function[149] and a 2×2 max-pooling layer.

A bottle-neck block with a similar structure, i.e., a 2D-convolution with 3×3 filter followed by a ReLu function, connects the encoder and the decoder sections. The decoder is also built with a repetitive structure of 6 decoding blocks. The first 4 decoder blocks consist of a 2×2 up-sampling layer, followed by an element-wise-sum residual layer[150] using skip connection[151] to the symmetrically matching encoder layer. Then, two successive processes of 3×3 2D convolution, and non-linear ReLu activation are performed. Owing to different resolution and sizes of the input images compared to the output images, two more decoding blocks are required, lacking the residual sum layers. The network final layer of a pixelwise prediction is performed by a single 1×1 filter 2D-convolution layer. Since a pixel-wise value prediction is required for the network output, a regression approach was adapted by minimizing the mean-squared-error (MSE) between the recovered HR image and the ground truth, and a weighted l_1 penalizer was added to promote the sparsity of the network output. The network implementation was done using Keras[152] with a TensorFlow[153] backend.

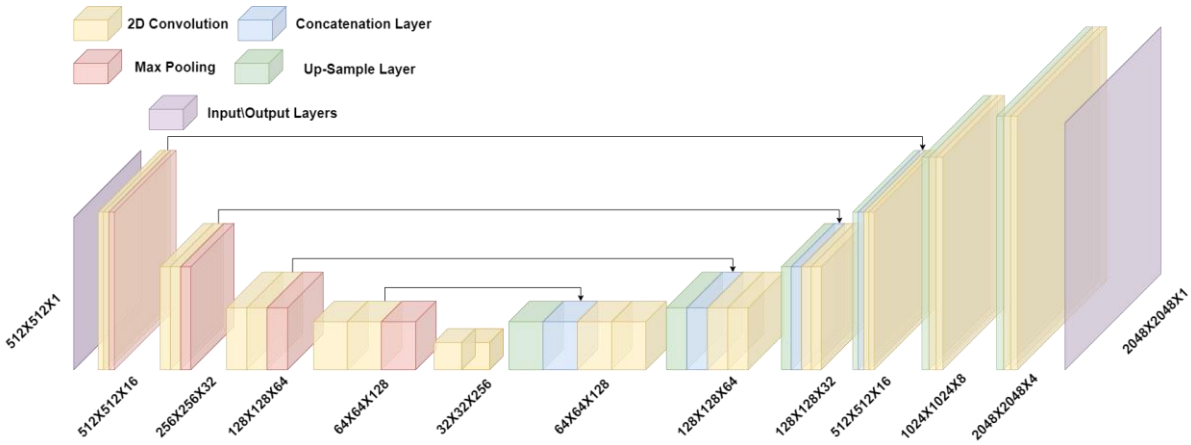

Figure 7. Network architecture, based on U-NET with two additional layers. Layer sizes noted below each block. Arrows mark skip connections between layers.

4.11. Network Optimization

Our network was optimized by two stages of parameters grid search. First, we focused on major architectural decisions, such as the hidden layers depth, convolution kernels size, and the use of batch normalization.[154] Second, we optimized the network hyper-parameters, including the batch-size, number of epochs, activation functions, kernel weights initializer, drop-out percentage coefficient, and the weight λ of the l_1 penalizer in the loss function.

4.11.1. Network architectural-parameters optimization

Our network was optimized by refining its architectural structure and parameters. Comparing a 9-layer network to 11- and 13-layer networks, we found that the deeper architectures resulted in better performance. Since the two extra layers in the 13-layer network provided no substantial improvement over the 11-layer network, the latter was chosen to reduce the number of weights, and to avoid encountering memory limitation errors (Figure 8a). Various 2D convolution kernel sizes were then tested to find an optimal kernel scale, where a 3X3 kernel was chosen as larger kernel sizes resulted in some blurring (Figure 8b). The validation loss and the peak signal-to-noise ratio (PSNR) value showed an almost monotonic decease during training, without batch normalization (Figure 8c). In contrast, batch normalization resulted in a wild fluctuation of the validation loss, attributed to the small batch size (which was limited by memory), as well as of the PSNR value, therefore, it was not used (Figure 8d).

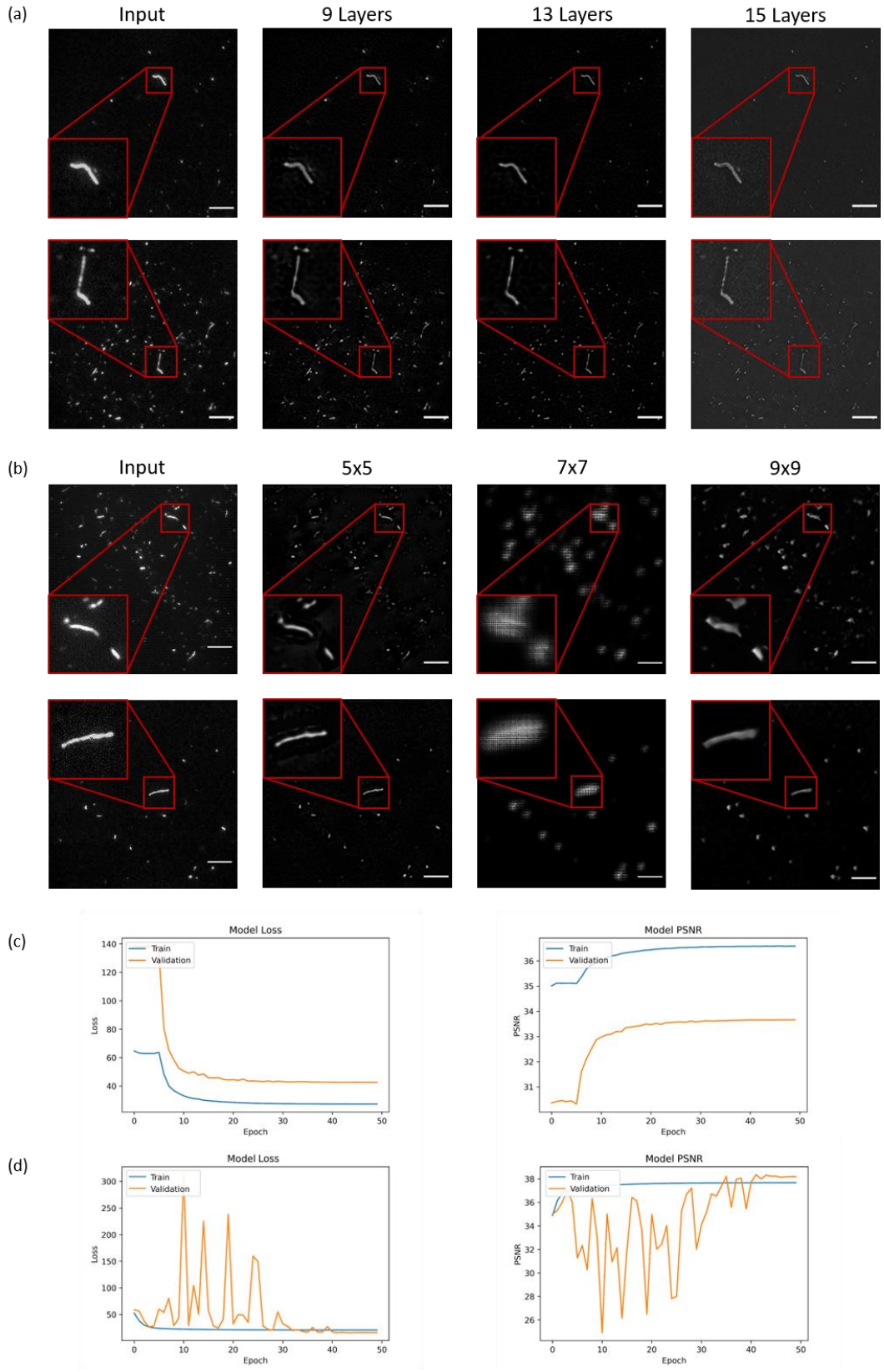

Figure 8. Parameters optimization visualization. Scale bar is 10 μm. a) Network results with different layer depths. b) Network results with different kernel sizes. c) Loss function and PSNR values without batch normalization. d) Loss function and PSNR values with batch normalization.

4.11.2. Network hyper-parameters optimization

The network optimizer, weights initializer, and activation function were set following an initial grid search over 450 different combinations. Various networks with specific parameter combinations were then ranked according to the mean PSNR value of the validation set. Subsequently, optimization of the hyper-parameters was done using a second grid-search of 150 combinations for 4 different parameters including the epoch number, batch size, drop-out factor value, and the weight λ of the l_1 penalizer in the loss function. Table 2 summarizes the values of the different parameters tested, and Table A1 in the appendix summarizes the combinations, ranked by their PSNR values. Final parameters of both grid searches were chosen as those which yielded the highest mean PSNR value of the validation set. Due to the relatively small number of images, the final network was trained on the entire dataset, i.e., both the training and validation images (total of 1192), to exploit all available data for the learning process. Following this final training, we tested our network performance on the test dataset. Final learning curves of this network represented by the loss and PSNR values can be seen in Figure 9.

Table 2. Network optimization hyper-parameters

Parameter	Tested	Chosen
Kernel initializer	He normal distribution [4], Glorot uniform distribution [5], Normal distribution, Uniform distribution, Zeros	He normal distribution
Activation Function	ReLu, Leaky ReLu	ReLu
Optimizer	Adam, Adam with decay learning	Adam with decay learning
Epoch number	50, 75, 100	100
Batch size	4, 8	8
Drop-out coefficient	0.0, 0.05, 0.1, 0.15, 0.2	0
L_1 penalizer weight λ	0.1, 0.25, 0.5, 0.75, 1.0	0.1

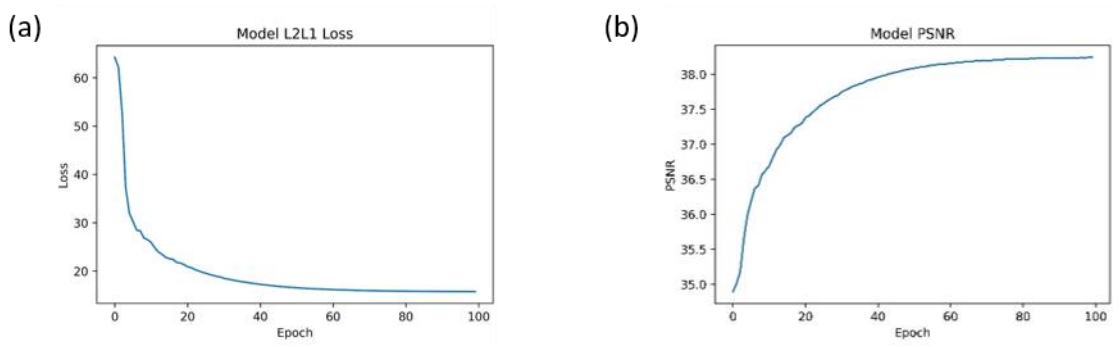

Figure 9. Final learning curves of the network. a) Loss function. b) PSNR values of the final network training.

4.12. Network training

The model performs supervised learning[155] using the 512×512 pixel-size LR input images and the 2048×2048 labeled SRRF images that serve as ground truth, and outputs HR images of the same size. The training was done using 1192 images, containing both long and short SWCNTs, to ensure the network can resolve all SWCNT length distribution concurrently. Adam optimizer[156] and decay-learning method[157] were used for adaptive optimization of the learning rate (initially set to 0.001) during the learning process. All kernel weights were initialized using a truncated normal distribution centered on 0, implemented by Keras 'He Normal' initializer.[158] We trained our network for 100 epochs with a batch size of 8. The PSNR, which is maximized by the minimization of our loss MSE function, is a common image quality measurement used to evaluate and compare SR models;[159] however, it is limited by its ability to capture perceptually relevant differences.[160–162] Therefore, PSNR was chosen as an evaluation metric and not as the network cost or optimization function. Training and evaluation were run on a standard workstation equipped with 32 GB of RAM memory, and a Nvidia GeForce RTX 2080 Ti GPU with 11 GB of memory. Full network training took 18 minutes.

5. Results and Discussion

5.1. SWCNT suspension characterization and imaging

SDBS-SWCNT suspensions were characterized by a UV-Vis-nIR absorption spectroscopy, where sharp absorption peaks indicated a successful suspension (Figure 10a). The nIR fluorescence emission spectra of SDBS-SWCNT were measured under a variety of excitation wavelengths showing distinguishable peaks corresponding to the different SWCNT chiralities in the suspension (Figure 10b).[33]

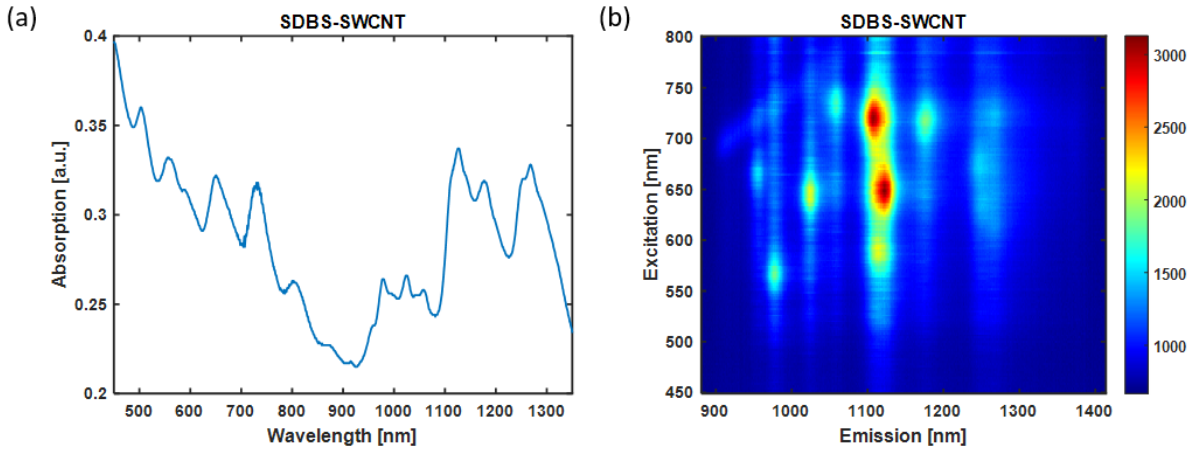

Figure 10. SDBS-SWCNT characterization. a) Absorption spectrum of SDBS-SWCNT. Presented results are of an SDBS-SWCNT suspension following 30 s sonication time, as suspension concentrations obtained from shorter sonication times were below the spectrophotometer threshold sensitivity. b) Excitation-emission map of SDBS-SWCNTs. Result shown are of a 10 s sonication suspension as a representative solution for the various sonication times.

To produce high SNR fluorescence images SDBS-SWCNT were immobilized on PLL-coated coverslips and imaged in TIRF mode in the nIR wavelength range (Figure 1b). Different incubation times of the negatively charged SDBS-SWCNT on the positively charged PLL-coated coverslips were used to vary the density of the immobilized SWCNTs. The coverslips were then mounted on an inverted nIR fluorescence microscope for TIRF imaging. The obtained 512×640 pixel images were first cropped to cubic images of 512×512 pixels and then processed by the SRRF algorithm, followed by manual

adjustments of background removal and contrast enhancement. Finally, the SRRF algorithm produced 2048×2048 super-resolution images, used as the GT for training our CNN (Figure 5a). Subsequently, and after separation by SWCNTs densities (high and low), all images were rotated and flipped horizontally as part of an augmentation process (Figure 6) to expand our resulted data set.

5.2. Network validation and testing

We used a CNN architecture, based on U-NET[139], to produce HR images of SWCNTs. U-NET, a CNN named after its symmetric U-shaped architecture of an encoder blocks follow by decoder blocks, was original introduced as a segmentation network. Contrary to the original U-NET, our network has an asymmetric architecture, with two ancillary decoding blocks that were added to the decoder, in addition to the 4 decoding blocks that are coupled to 4 corresponding encoding blocks by skip connections to provide larger output images (2048×2048) from the input frames (512×512).

Following the network supervised training using the SRRF 2048×2048 HR images as our desired GT, we validated our network on 100 images, which were chosen randomly with the same density distribution as the initial data set. The resolution improvement for the test set was quantified using the FWHM criterion, calculated from a standard Gaussian fit to a cross-section of 10 random SWCNTs in one representative image for each image category (e.g., low and high density), for all three images types (i.e., input image, SRRF image, and the network predicted image). In order to compare the resolution, we calculated the FWHM of the input image, the SRRF GT, and the HR predicted output (Table 3). The quality of predicted images was evaluated from the SNR values, which were calculated based on 5 images for each image category. Both FWHM and SNR values

are shown in Table 3, including the improvement factor compared to the original LR images.

Table 3. Resolution and image quality parameters

Image	Evaluation Parameter	LR	SRRF	HR	SRRF Improvement [%]	Network Improvement [%]
Low Density	FWHM [μm]	0.95±0.11	0.66±0.09	0.74±0.02	29.6±13.1	21.1±7.6
	SNR [dB]	28.4±1.3	34.7±0.8	42.1±0.8	22.4±5.8	48.7±7.5
High Density	FWHM [μm]	0.95±0.06	0.66±0.03	0.73±0.02	30.7±6.7	22.7±5.4
	SNR [dB]	28.4±1.1	35.6±0.9	40.1±1.7	25.7±8.1	47.4±5.8
Short SWCNTs	FWHM [μm]	1.1±0.2	0.8±0.1	0.78±0.06	28.5±22.7	27.4±16.6
	SNR [dB]	29.3±0.4	33.9±0.7	42.4±0.5	15.7±4.1	44.8±2.5
Long SWCNTs	FWHM [μm]	0.95±0.07	0.75±0.1	0.77±0.04	20.5±15.4	18.5±7.0
	SNR [dB]	28.3±1.1	34.9±1.8	41.8±1.5	23.3±5.4	47.9±6.1

We first tested our network performance on images with varying SWCNT densities (Figure 11a, b). The averaged FWHM values of the fluorescent SWCNTs in the low density LR images were 0.95 ± 0.11 μm while the HR FWHM values were 0.74 ± 0.02 μm. Although the overall background brightness of the dense images is higher compared to the sparse, low-density images, the network could resolve individual SWCNT in higher densities as well, resulting in an improvement of the averaged FWHM values which were 0.95 ± 0.06 μm and 0.73 ± 0.02 μm for LR and HR images in the high-density images, respectively.

Moreover, we tested our network performance on images with both short and long (up to 10 μm) SWCNTs (Figure 11c, d). FWHM values of the LR images were 1.1 ± 0.25 μm and 0.95 ± 0.07 μm, for short and long SWCNTs images respectively, whereas the predicted HR images FWHM values were 0.78 ± 0.06 μm and 0.77 ± 0.04 μm respectively. Although long SWCNTs can be twisted and curled, our network managed

to successfully predict HR SWCNTs images for both long and short SWCNTs and is not limited to resolving only spherical or cylindrical shapes.

Overall, we showed $21 \pm 7\%, 22 \pm 5\%, 27 \pm 16\%$ and $18 \pm 7\%$ improvements in the FWHM values of the SWCNTs in the predicted HR images, compared to the LR images, for the low-density, high-density, short, and long SWCNT images, respectively, which are all statistically significant results (Figure 11e). Similar improvement values were obtained for the SRRF images compared to the LR images, showing no statistically significant difference between the SRRF and predicted-HR images (Figure 11f).

With an overall average FWHM improvement of $22 \pm 9\%$ compared to the input image, and an increase in the SNR values of all HR images compare to the LR images (Table 3), we successfully showed improvement in both the resolution and quality of the images across a range of different SWCNTs lengths and densities.

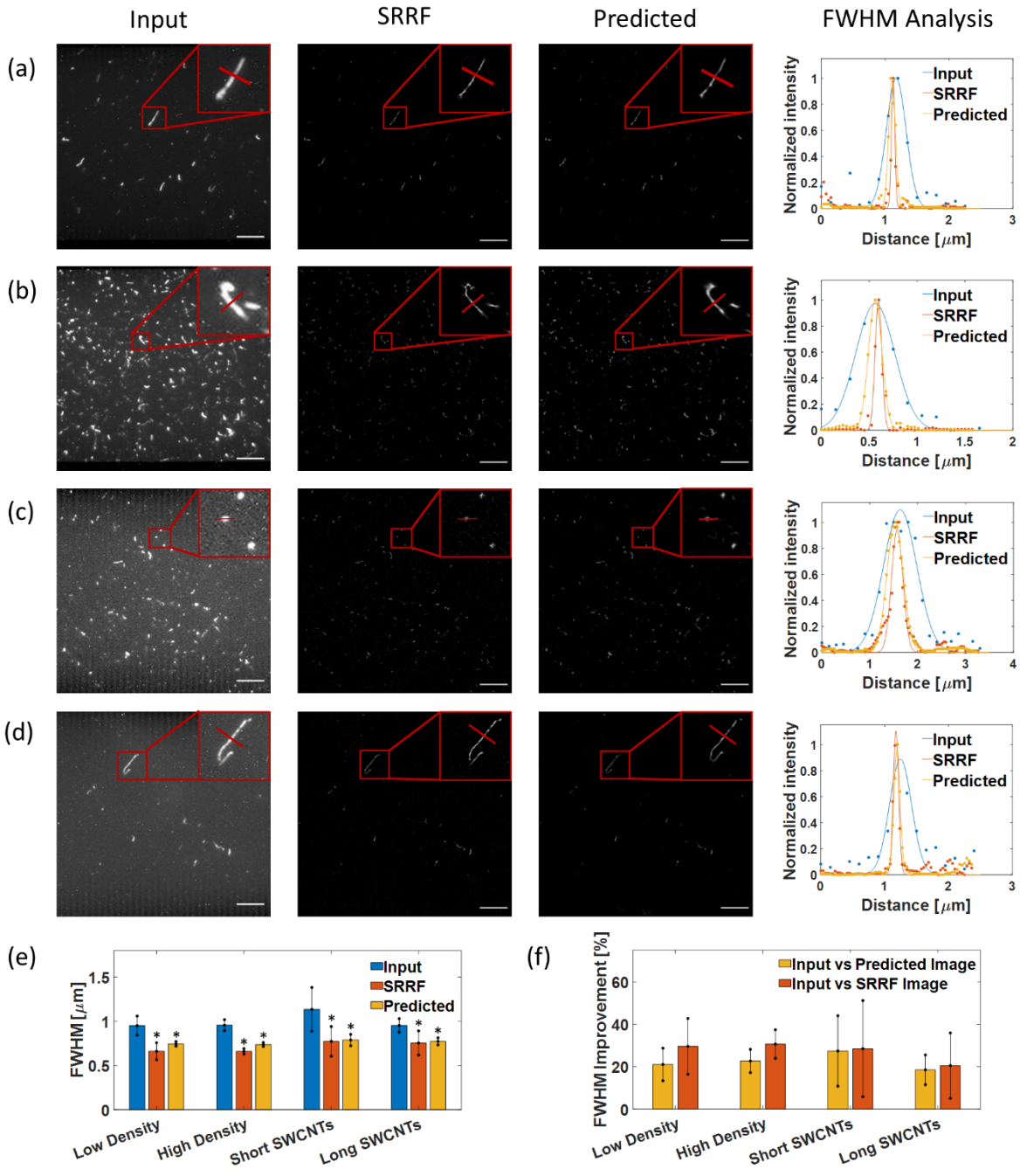

Figure 11. Network results compared to the SRRF algorithm. Red lines represent the cross section used for calculating the FWHM of individual SWCNTs. Each row represents different image properties. From left to right: original TIRF image input, SRRF output, network output, and FWHM analysis based on the intensity cross-section of SWCNTs marked in red lines fitted by a gaussian. Scale bar stands for 10 μm a) Low density SWCNTs image. b) High density SWCNTs image. c) Short SWCNTs image. d) Long SWCNTs image. e) Mean FWHM calculated for 10 individual SWCNTs from each image type. * Represents a statistically significant difference compared to the input LR images (*P < 0.01). f) Improvement factor of the FWHM value compared to the LR TIRF input images.

To further challenge the reconstruction performance of our network, we tested complex imaging conditions such as low SNR, high-intensity-background images, as well as images with SWCNTs in close proximity with spatially overlapping fluorescence. In the case of poor SNR and noisy, bright background, our network showed a FWHM value improvement of $33 \pm 12\%$ (Figure 12a) and an SNR improvement of $47 \pm 5\%$, demonstrating that our network can remove backgrounds, thus improving the contrast and sharpness of the predicted image. Further, we successfully demonstrated the separation of two neighboring SWCNTs (Figure 12b), where the normalized ratio of the maximum intensity peak and the minimum intensity value between the peaks improved from 0.6 to 1. Upon closer inspection of the FWHM analysis plots (Figure 11a-d, Figure 12a, b), the gaussian fit of the intensity cross-section in the SRRF outputs and the network predicted images nearly overlap, further exemplifying the successful learning process of our network given the SRRF GT. Nevertheless, there are some cases in which the two gaussians differ, such as in Figure 12b, where a local maximum appears between the two main peaks only in the SRRF output. This difference is attributed to 'edge' artifacts in the SRRF algorithm[108] that may cause two separate SWCNTs to appear connected when in fact they are merely adjacent, and will be further discussed in the following section.

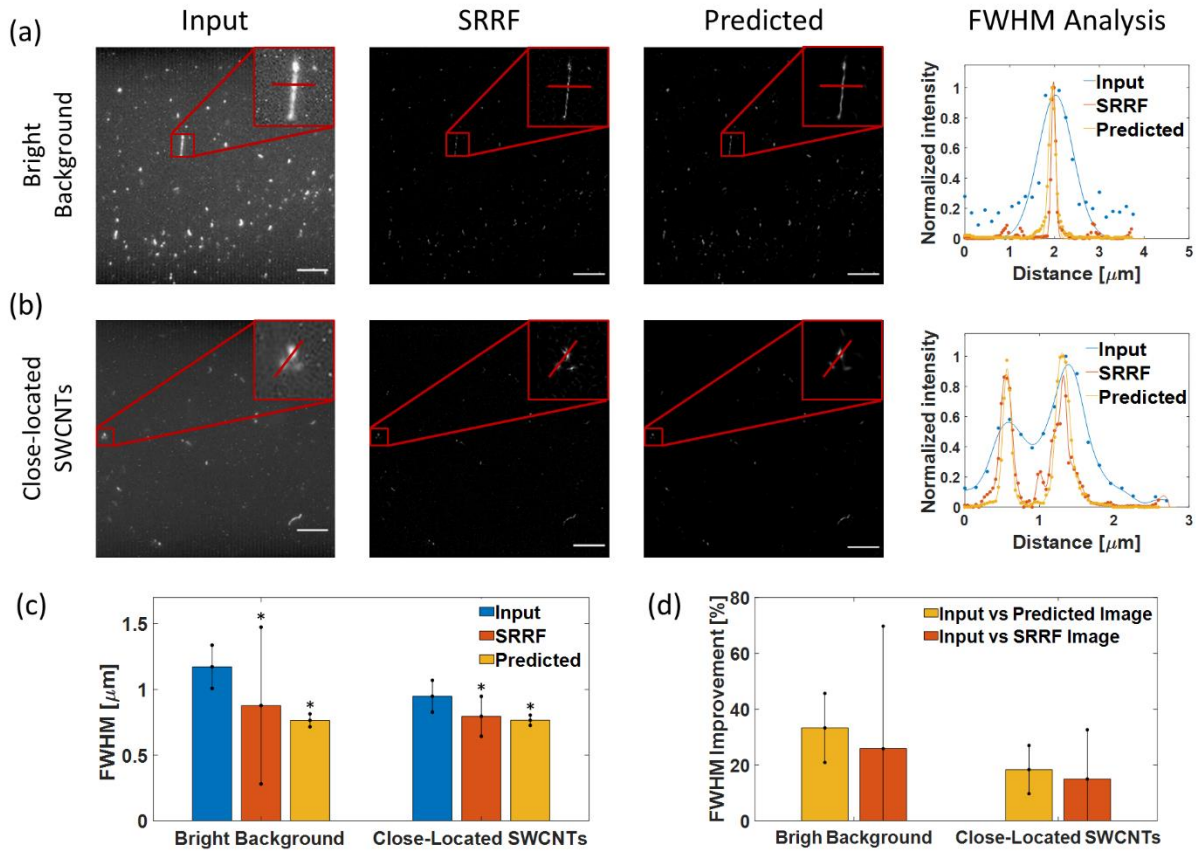

Figure 12. Network performance for complex imaging conditions. Scale bar stands for 10 μm a) Bright background with low SNR TIRF image, its corresponding SRRF GT, network predicted image and a comparable FWHM analysis for all three images. b) TIRF image of SWCNTs in close proximity with overlapping fluorescence, its corresponding SRRF GT, the network predicted image and a comparable FWHM analysis for all three images. c) Mean FWHM calculated for 10 corresponding individual SWCNTs in all three images. * Represents a statistically significant difference compared to the input LR images (*P < 0.01). d) Improvement factor of the FWHM value for every image compared to the LR TIRF input images.

The peak signal to noise ratio (PSNR) value is commonly used as a quantitative measure of image reconstruction quality in deep-learning-based SR models, where a higher PSNR generally indicates a reconstruction of higher quality. We have calculated the PSNR values of all image categories by averaging over 5 output images per category, compared to the GT images of the SRRF algorithm (Table 4).

Table 4. PSNR values of predicted images compared to the GT SRRF images

Image category	Low Density	High Density	Short SWCNTs	Long SWCNTs	Low SNR (high background)	Closely-located SWCNTS
PSNR [dB]	36.6 ± 1.3	30.5 ± 0.7	30.4 ± 1.1	31.5 ± 3.6	30.9 ± 0.1	26.1 ± 2.8

5.3. Super-resolution of videos

In a previous study[108] we demonstrated improved resolution of videos using the SRRF algorithm, and showed that it could capture the bending dynamics[12] of diffusing SWCNTs and their mean-square displacement. However, since SRRF uses temporal correlation within the radiality stack to create the final SRRF image,[86,117] the temporal resolution was decreased since 10 consecutive frames were used by the SRRF algorithm to produce a single super-resolved frame in the video output. Figure 13a shows snapshots taken from a video of SWCNTs, and their corresponding HR output images of our network. Due to our network ability to resolve single frames without the need for temporal information nor preprocessing, our approach provides high resolution videos, frame-by-frame, in real-time, with the same temporal resolution as the input video.

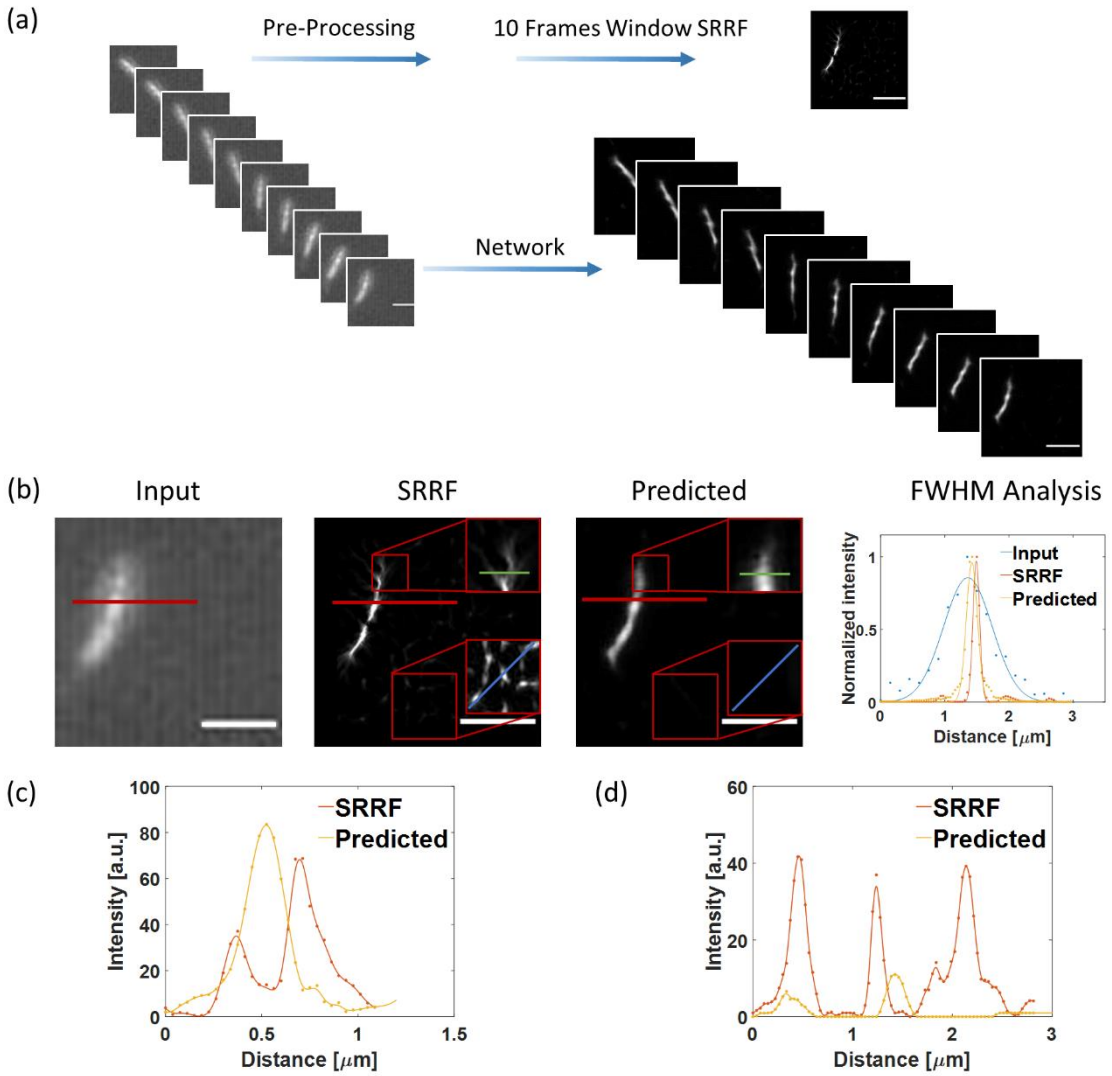

Figure 13. Super-resolved video frames. Scale bar stands for 2 μm a) Representative comparison of both SRRF and CNN methods shows the difference in temporal resolution and the number of extracted frames. b) Snapshot from the original video, its corresponding SRRF resolved image, the network predicted image, and a comparable FWHM analysis for all three images, based on the solid red line. c) Pixels intensity analysis for 'edge' artifacts, corresponding to the green lines. d) Comparable pixels-intensity analysis for the background artifacts, corresponding to the blue lines.

The FWHM value of the input LR frame (Figure 13b) is 1.16 μm, and while the FWHM values of the SRRF and the HR predicted images are 0.71 μm and 0.78 μm, respectively. Two substantial issues are worth mentioning regarding 'edge' and background artifacts. First, Figure 13c shows the intensity along the green lines in the SRRF and predicted

images in Figure 13b, demonstrating the ‘edge’ artifact in the SRRF algorithm. The edge of the SWCNTs seems to be split at its end in the SRRF image, whereas the predicted image shows a more uniform, single edge. This effect has crucial implications, especially when there are two nearby adjacent SWCNTs that may be interpreted as connected, therefore distorting the information in the resolved image.

Second, the SRRF output image tends to suffer from more background noise. Figure 13d shows the intensity along the blue lines in the background region of the SRRF and predicted images in Figure 13b. These background regions were contrast-enhanced for ease of visualization in the enlarged areas in Figure 13b, but the intensity profiles in Figure 13d were extracted from the actual pixel values of both images. Comparing the SRRF and the predicted images, the latter benefits from significantly lower intensity values of the background pixels, which are hardly noticeable by the naked eye. Hence, our network can improve the spatial resolution and preserve the temporal resolution without the emergence of edges or background artifacts, thereby providing higher SNR.

5.4. Network validation on non-nIR images

So far, all validated images were taken with an InGaAs-based nIR camera to capture the diverse set of SWCNTs chiralities in our samples. Since SWCNTs emission wavelengths are in the nIR range, using an InGaAs camera provides optimal detection of the SWCNTs fluorescence. In order to demonstrate that no specialized optical equipment is needed for using our method, we further tested our network performance with fluorescence images taken with a silicon-based EMCCD visible camera, which is more commonly used in optic labs for fluorescence emitters in the visible range. The visible images were taken with the same setup, by switching the 900 nm long-pass dichroic mirror that directs fluorescence emission <900 nm to the visible camera (and fluorescence emission >900

nm to the nIR camera), with an 1100 nm long-pass dichroic mirror that directs fluorescence emission <1100 nm to the visible camera. While the nIR camera has a quantum efficiency (QE) of >65% at 900 nm and >85% between 1000-1500 nm, and can therefore detect a wide range of SWCNT chiralities, the EMCCD camera has a QE of 40% at 900 nm which drops down to 0% at 1100 nm. Still, SWCNTs chiralities that fluoresce in the range of 900-1100 nm could be detected by the visible camera. Figure 14a shows images of the same sample taken by both cameras, clearly showing a few SWCNTs appearing in both images. We then tested the network performance on the visible-range images compared to the corresponding nIR range images (Figure 14b). In a similar manner to the results in Figure 11 and Figure 12, the resolution improvement was quantified using the FWHM values, extracted from a standard gaussian fit to a cross-section of 3 randomly selected SWCNTs from 5 different images with the visible camera and their equivalent SWCNTs taken with the nIR camera. The averaged FWHM values of the fluorescent SWCNTs prior to the network implementation, presented in Figure 14c, were 0.75±0.03 μm and 0.74±0.03 μm for the visible and nIR cameras, respectively. The corresponding FWHM values of the SWCNT in the HR network output images were 0.55±0.02 μm and 0.55±0.01 μm, showing FWHM improvement of 26±4.1% and 26±2.9% for the visible and nIR cameras, respectively, similar to the previous results. These results demonstrate the applicability of our network to fluorescence images of SWCNTs taken with a visible camera, without specialized optical components.

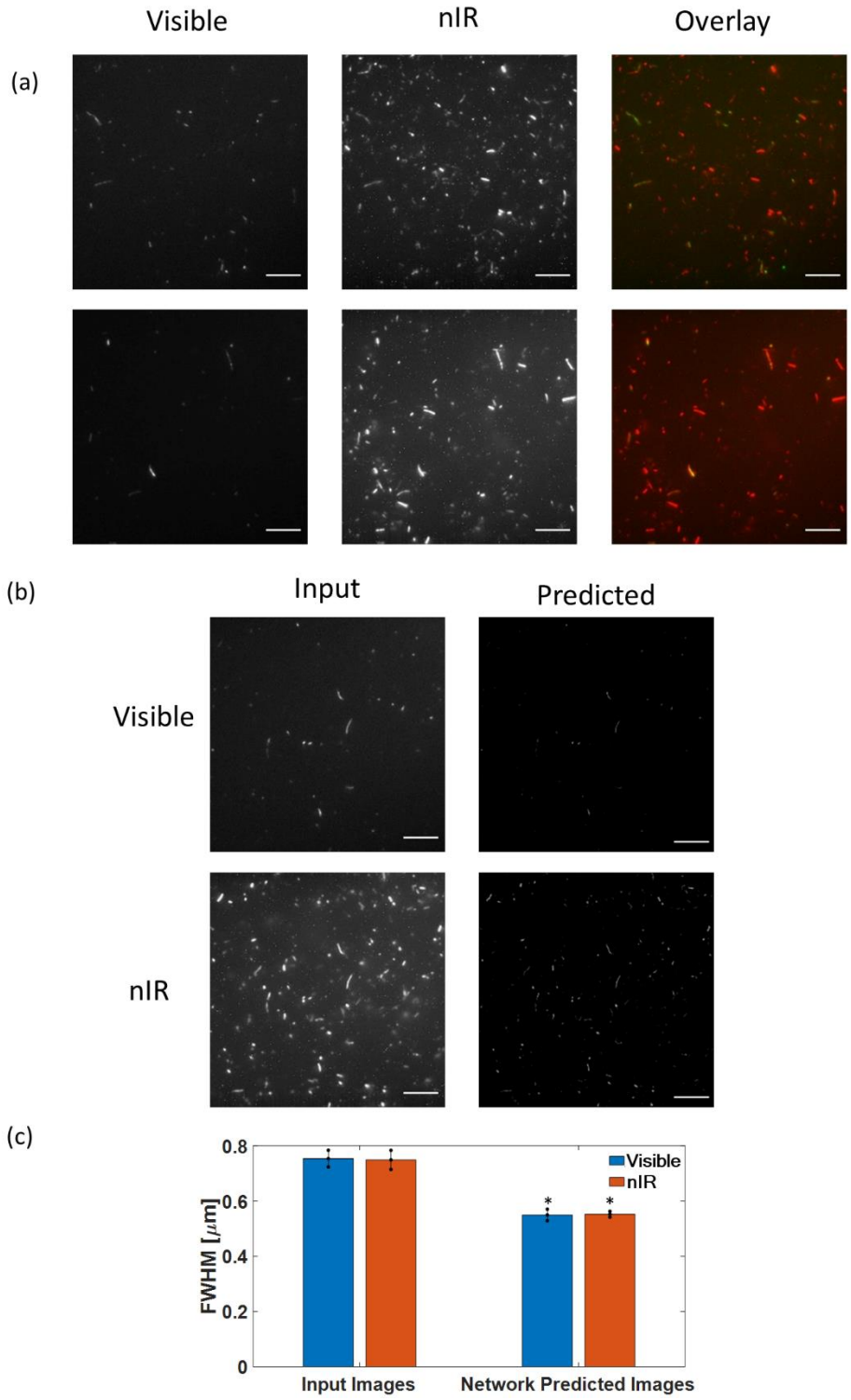

Figure 14. Network implementation on EMCCD camera images. Scale bars stand for 10 µm. a) Comparison between the fluorescence images in the visible range camera, the nIR camera, and an overlay image of both (visible in green, nIR in red). b) Image of the same sample taken with both cameras, and their corresponding network predicted output. c) Mean FWHM calculated for 15 individual SWCNTs. *Represents a statistically significant difference compared to the input LR images (*$P < 0.01$).

6. Conclusion and summary

Super-resolution (SR) techniques enhance our understanding of precise structural features and dynamic behaviors at the nano-scale. Applied to near-infrared fluorescence imaging, SR approaches further benefit from reduced absorption, scattering, and autofluorescence in the biological transparency window.[28,72–74] SWCNTs in particular are advantageous nIR fluorescent probes owing to their photostable, non-photobleaching, non-blinking fluorescence in the range of 900 – 1400 nm.[30,42,43] Moreover, their physical and chemical properties, along with the ease of surface functionalization, render them favorable optical sensors for biomedical applications.[19,20,31]

In this work, I have shown the advantages of deep learning via a novel, U-NET based CNN architecture holding asymmetric properties, for SR of fluorescence imaging in the nIR by demonstrating the improved resolution and SNR of SWCNT images, without the need for specialized imaging equipment or parameters tuning. I validated the use of the network on challenging imaging conditions such as low SNR images and adjacent SWCNTs with overlapping fluorescence, as well as diverse scenarios such as different SWCNT densities and lengths, that were achieved by creating and refining new suspension protocols, involving varying ultra-short sonication times and a two-stage centrifuging protocol to offer uncommonly long SWCNT. I have demonstrated an average spatial-resolution improvement of 22.4% compared to the original images and an image-quality improvement, reflected by the SNR values, over both the original and SRRF images in all cases. It is worthy of note that previous research done in our lab[108] on SRRF implementation for nIR fluorescence images of SWCNT showed an average improvement of 78.26% of the FWHM values, yet in the current work, I have optimized our imaging setup so the initial FWHM values of the SWCNTs in the LR images were

much smaller. Such optimization was obtained by the innovative combination of two protocols – through the immobilization of SWCNT on a PLL coated cover slip relying on opposite electrical charges, the TIRF imaging protocol yielded better results than were in our lab up to this point as only the immobilized SWCNTs were excited in the interference layer, while the rest of the unattached SWCNTs in the sampled were excited by the exponentially attenuated evanescence field, hence resulting less background noise and better SNR. Furthermore, the SNR improvement was found higher in the network predicted images by an average of 47% compared to 24% for the SRRF outputs. This difference can be attributed to background noises and 'edge' artifacts (Figure 13c, d) that appear mostly at the SWCNTs ends when using SRRF method which are absent in the network predicted images, and I have also demonstrated an improvement in the temporal-resolution for SR of videos compared to SRRF. Although the spatial-resolution of the networks' super-resolved images is still limited by the resolution of the SRRF GT, my method shows significant advantages being parameter-free, requires no multi-frame temporal information, produces no visible artifacts in the output images and having a faster running of 0.75±0.002 s on average (with optional automatic pre-processing of 4.5±0.09 s for background removal), compared to 38±2 s in the case of SRRF.

With the purpose of highlighting this model advantages over other super-resolution microscopy techniques and to prove that no specialized optical components are required, I have demonstrated the applicability of my network on images of SWCNTs taken with a common silicon-based EMCCD camera in contrast to the InGaAs-based nIR camera, showing promising results of our network on visible range images that share the same standards as the results of the nIR images.

Nonetheless, the network performances were affected by the relatively small size of the training dataset dictated by the complexity of experimentally obtaining the images. Some

of the plausible courses of action can be either utilization of suitable manipulations considering the size of the dataset, such as k-fold cross validation techniques. Cross-validation is a resampling method that uses different portions of the data to test and train a model on different iterations. As this technique averages-out measures of fitness in prediction model, one can derive a more accurate estimate of model prediction performance, especially under small dataset that offers little certainty regarding the networks results. Another approach may come simply through the enlargement of the experimental data, but since that option was neglected due to time constraints one can also generate high-quality synthetic data. Nevertheless, producing synthesized SWCNTs data compared to other simulated dot emitters, encompasses additional aspects, including the shape, bending, and chirality dynamics as well as non-uniform emission properties of the imaged material, alongside the synthesis of background conditions similar to real imaging conditions. Owing to the difficulties mentioned in generating such high-complexity data, this subject is a future field of research in the Bisker lab. Such simulated data will not only increase the amount of training data, but will also enable a quantitative assessment of the precision in the predicted location of the SWCNT in the network output image. Taking advantage of transfer learning can also be employed in use-cases where only small amounts of data are available. By reusing pre-trained model weights, and fine-tuning it for a new problem in hand, namely super resolution, one can benefit from saving training time, and to not relay on a big data set, such as in our case.

Despite the relatively small database, I believe this current model will already prove useful in assorted applications. For example, an upcoming study that develops a microchip consist of an array of immobilized functionalized SWCNTs, will allow the re-binding of given SWCNTs to different analytes that will be pumped into and washed off the microchip. While the development will allow the reuse of functionalized SWCNTs

and measurements regarding the fluorescence modulation the probes will exhibit upon interaction with different analytes, the usage of my model will enable further investigation of the individual SWCNT behavior once interacted with the said material. Even further, future research that will be conducted in various biological environments such as within cells or even small multicellular organise such as caenorhabditis elegans will now have the ability to better track a single particle through space without compromising temporal information, and thus to offer a more accurate image of a singular SWCNT diffusing dynamics. In contrast to the aforementioned future uses, which relay on the development of new research methods, an almost immediate use for my network is the reconstruction of super-resolution studies using SWCNTs as imaging probes (mentioned in the chapter 2.1.2), benefiting from shorter calculation times and better temporal resolution, which will enable an easier reproduction of such studies and thereby accelerate the study of biological environments topographies.

In summary, being fast, parameter-free, and robust for various imaging conditions, my CNN-based approach for resolving nIR fluorescence images of SWCNTs is highly attractive as a super-resolution method. Given its simplicity and robustness, combined with nIR fluorescent SWCNTs, this model paves the way to sub-diffraction super-resolved imaging in the nIR in real-time, opening a window to nanoscale structures in biological environment.

References

[1] S. Kruss, A. J. Hilmer, J. Zhang, N. F. Reuel, B. Mu, M. S. Strano, *Adv. Drug Deliv. Rev.* **2013**, *65*, 1933.

[2] J. T. D. Bonis-O'Donnell, R. H. Page, A. G. Beyene, E. G. Tindall, I. R. McFarlane, M. P. Landry, *Adv. Funct. Mater.* **2017**, *27*, 1702112.

[3] R. Ehrlich, A. Hendler-Neumark, V. Wulf, D. Amir, G. Bisker, *Small* **2021**, *17*, 6511.

[4] P. W. Barone, S. Baik, D. A. Heller, M. S. Strano, *Nat. Mater.* **2005**, *4*, 86.

[5] G. Bisker, J. Dong, H. D. Park, N. M. Iverson, J. Ahn, J. T. Nelson, M. P. Landry, S. Kruss, M. S. Strano, *Nat. Commun.* **2016**, *7*, 10241.

[6] G. Bisker, N. A. Bakh, M. A. Lee, J. Ahn, M. Park, E. B. O'Connell, N. M. Iverson, M. S. Strano, *ACS Sensors* **2018**, *3*, 367.

[7] V. Wulf, G. Slor, P. Rathee, R. J. Amir, G. Bisker, *ACS Nano* **2021**, *15*, 20539.

[8] D. Amir, A. Hendler-Neumark, V. Wulf, R. Ehrlich, G. Bisker, *Adv. Mater. Interfaces* **2022**, *9*, 59.

[9] V. Zubkovs, A. Antonucci, N. Schuergers, B. Lambert, A. Latini, R. Ceccarelli, A. Santinelli, A. Rogov, D. Ciepielewski, A. A. Boghossian, *Sci. Rep.* **2018**, *8*, 13770.

[10] H. Wu, R. Nißler, V. Morris, N. Herrmann, P. Hu, S. J. Jeon, S. Kruss, J. P. Giraldo, *Nano Lett.* **2020**, *20*, 2432.

[11] P. V Jena, M. Gravely, C. Cupo, M. M. Safaee, D. Roxbury, D. A. Heller, *ACS Nano* **2022**, *16*, 3104.

[12] N. Fakhri, D. A. Tsyboulski, L. Cognet, R. B. Weisman, M. Pasquali, R. Bruce Weisman, M. Pasquali, *PNAS* **2009**, *106*, 14219.

[13] T. H. Tan, M. Malik-Garbi, E. Abu-Shah, J. Li, A. Sharma, F. C. MacKintosh, K. Keren, C. F. Schmidt, N. Fakhri, *Sci. Adv.* **2018**, *4*, eaar2847.

[14] N. Fakhri, F. C. MacKintosh, B. Lounis, L. Cognet, M. Pasquali, *Science* **2010**, *330*, 1804.

[15] Z. Hou, T. M. Tumiel, T. D. Krauss, *J. Appl. Phys.* **2021**, *129*, 014305.

[16] V. Shumeiko, Y. Paltiel, G. Bisker, Z. Hayouka, O. Shoseyov, *Sensors (Switzerland)* **2020**, *20*, 1.

[17] V. Shumeiko, Y. Paltiel, G. Bisker, Z. Hayouka, O. Shoseyov, **2021**, *172*, 112763.

[18] V. Shumeiko, E. Malach, Y. Helman, Y. Paltiel, G. Bisker, Z. Hayouka, O. Shoseyov, *Sensors Actuators, B Chem.* **2021**, *327*, 128832.

[19] A. Hendler-Neumark, V. Wulf, G. Bisker, *Mater. Today Bio* **2021**, *12*, 100175.

[20] J. Ackermann, J. T. Metternich, S. Herbertz, S. Kruss, *Angew. Chemie - Int. Ed.* **2022**, *61*, e202112372.

[21] E. M. Hofferber, J. A. Stapleton, N. M. Iverson, *J. Electrochem. Soc.* **2020**, *167*, 037530.

[22] V. Shumeiko, Y. Zaken, G. Hidas, Y. Paltiel, G. Bisker, O. Shoseyov, *IEEE Sens. J.* **2022**, *22*, 6277.

[23] D. P. Salem, M. P. Landry, G. Bisker, J. Ahn, S. Kruss, M. S. Strano, *Carbon N. Y.* **2016**, *97*, 147.

[24] V. B. Koman, N. A. Bakh, X. Jin, F. T. Nguyen, M. Son, D. Kozawa, M. A. Lee, G. Bisker, J. Dong, M. S. Strano, *Nat. Nanotechnol.* **2022**, DOI 10.1038/s41565-022-01136-x.

[25] R. Duggal, M. Pasquali, *Phys. Rev. Lett.* **2006**, *96*, 246104.

[26] F. N. Soria, C. Paviolo, E. Doudnikoff, M. L. Arotcarena, A. Lee, N. Danné, A. K. Mandal, P. Gosset, B. Dehay, L. Groc, L. Cognet, E. Bezard, *Nat. Commun.* **2020**,

11, 3440.

[27] A. G. Godin, J. A. Varela, Z. Gao, N. Danné, J. P. Dupuis, B. Lounis, L. Groc, L. Cognet, *Nat. Nanotechnol.* **2017**, *12*, 238.

[28] S. Nandi, K. Caicedo, L. Cognet, *Nanomaterials* **2022**, *12*, 1433.

[29] A. Hendler-Neumark, G. Bisker, *Fluorescent Single-Walled Carbon Nanotubes for Protein Detection*, MDPI AG, **2019**.

[30] S. Weiss, *PNAS* **2000**, *97*, 8747.

[31] M. M. Alvarez, J. Aizenberg, M. Analoui, A. M. Andrews, G. Bisker, E. S. Boyden, R. D. Kamm, J. M. Karp, D. J. Mooney, R. Oklu, D. Peer, M. Stolzoff, M. S. Strano, G. Trujillo-De Santiago, T. J. Webster, P. S. Weiss, A. Khademhosseini, D. Peer, M. Stolzoff, M. S. Strano, G. Trujillo-De Santiago, T. J. Webster, P. S. Weiss, A. Khademhosseini, *ACS Nano* **2017**, *11*, 5195.

[32] B. Kagan, A. Hendler-Neumark, V. Wulf, D. Kamber, R. Ehrlich, G. Bisker, *Adv. Photonics Res.* **2022**, *3*, 2200244.

[33] S. M. Bachilo, M. S. Strano, C. Kittrell, R. H. Hauge, R. E. Smalley, R. B. Weisman, *Science* **2002**, *298*, 2361.

[34] K. Fujita, M. Fukuda, S. Endoh, H. Kato, J. Maru, A. Nakamura, K. Uchino, N. Shinohara, S. Obara, R. Nagano, M. Horie, S. Kinugasa, H. Hashimoto, A. Kishimoto, *Toxicol. Mech. Methods* **2013**, *23*, 598.

[35] W. Zhou, X. Bai, E. Wang, S. Xie, *Adv. Mater.* **2009**, *21*, 4565.

[36] O. Moradi, M. Yari, K. Zare, B. Mirza, F. Najafi, *Fullerenes, Nanotub. Carbon Nanostructures* **2011**, *20*, 138.

[37] S. Settele, F. J. Berger, S. Lindenthal, S. Zhao, A. A. El Yumin, N. F. Zorn, A. Asyuda, M. Zharnikov, A. Högele, J. Zaumseil, *Nat. Commun.* **2021**, *12*, 2119.

[38] Z. Yao, C. C. Zhu, M. Cheng, J. Liu, *Comput. Mater. Sci.* **2001**, *22*, 180.

[39] T. C. Dinadayalane, J. Leszczynski, in *Handb. Comput. Chem.*, Springer Science, Business Media Dordrecht, **2016**, pp. 1–84.

[40] M. J. O'Connell, S. H. Bachilo, C. B. Huffman, V. C. Moore, M. S. Strano, E. H. Haroz, K. L. Rialon, P. J. Boul, W. H. Noon, C. Kittrell, J. Ma, R. H. Hauge, R. B. Weisman, R. E. Smalley, *Science* **2002**, *297*, 593.

[41] M. P. Landry, L. Vuković,Vuković, S. Kruss, G. Bisker, A. M. Landry, S. Islam, R. Jain, K. Schulten, M. S. Strano, *J. Phys. Chem. C* **2015**, *119*, 28.

[42] N. M. Iverson, P. W. Barone, M. Shandell, L. J. Trudel, S. Sen, F. Sen, V. Ivanov, E. Atolia, E. Farias, T. P. McNicholas, N. Reuel, N. M. A. Parry, G. N. Wogan, M. S. Strano, *Nat. Nanotechnol.* **2013**, *8*, 873.

[43] A. A. Boghossian, J. Zhang, P. W. Barone, N. F. Reuel, J. H. Kim, D. A. Heller, J. H. Ahn, A. J. Hilmer, A. Rwei, J. R. Arkalgud, C. T. Zhang, M. S. Strano, *ChemSusChem* **2011**, *4*, 848.

[44] S. Wray, M. Cope, D. T. Delpy, J. S. Wyatt, E. O. R. Reynolds, *BBA - Bioenerg.* **1988**, *933*, 184.

[45] N. M. Iverson, G. Bisker, E. Farias, V. Ivanov, J. Ahn, G. N. Wogan, M. S. Strano, *J. Biomed. Nanotechnol.* **2016**, *12*, 1035.

[46] S. Zhu, F. Luo, J. Li, B. Zhu, G. X. Wang, *J. Nanobiotechnology* **2018**, *16*, 44.

[47] T. V Galassi, M. Antman-PassigID, Z. Yaari, J. Jessurun, R. E. Schwartz, D. A. Heller, *PLoSONE* **2020**, *15*, DOI 10.1371/journal.pone.0226791.

[48] Z. Liu, C. Davis, W. Cai, L. He, X. Chen, H. Dai, *Proc. Natl. Acad. Sci. U. S. A.* **2008**, *105*, 1410.

[49] Z. Liu, W. Cai, L. He, N. Nakayama, K. Chen, X. Sun, X. Chen, † And, H. Dai, *Nat. Nanotechnol.* **2006**, *2*, 47.

[50] S. Y. Kwak, T. T. S. Lew, C. J. Sweeney, V. B. Koman, M. H. Wong, K. Bohmert-

Tatarev, K. D. Snell, J. S. Seo, N. H. Chua, M. S. Strano, *Nat. Nanotechnol.* **2019**, *14*, 447.

[51] M. H. Wong, J. P. Giraldo, S. Y. Kwak, V. B. Koman, R. Sinclair, T. T. S. Lew, G. Bisker, P. Liu, M. S. Strano, *Nat. Mater.* **2017**, *16*, 264.

[52] M. C. Y. Ang, N. Dhar, D. T. Khong, T. T. S. Lew, M. Park, S. Sarangapani, J. Cui, A. Dehadrai, G. P. Singh, M. B. Chan-Park, R. Sarojam, M. Strano, *ACS Sensors* **2021**, *6*, 3032.

[53] P. Cherukuri, C. J. Gannon, T. K. Leeuw, H. K. Schmidt, R. E. Smalley, S. A. Curley, R. B. Weisman, *Proc. Natl. Acad. Sci. U. S. A.* **2006**, *103*, 18882.

[54] K. Welsher, Z. Liu, D. Daranciang, H. Dai, *Nano Lett.* **2008**, *8*, 586.

[55] M. Gravely, M. M. Safaee, D. Roxbury, *Nano Lett.* **2019**, *19*, 6203.

[56] T. V. Galassi, P. V. Jena, J. Shah, G. Ao, E. Molitor, Y. Bram, A. Frankel, J. Park, J. Jessurun, D. S. Ory, A. Haimovitz-Friedman, D. Roxbury, J. Mittal, M. Zheng, R. E. Schwartz, D. A. Heller, *Sci. Transl. Med.* **2018**, *10*, eaar2680.

[57] D. Meyer, S. Telele, A. Zelená, A. J. Gillen, A. Antonucci, E. Neubert, R. Nißler, F. A. Mann, L. Erpenbeck, A. A. Boghossian, S. Köster, S. Kruss, *Nanoscale* **2020**, *12*, 9104.

[58] K. Welsher, Z. Liu, S. P. Sherlock, J. T. Robinson, Z. Chen, D. Daranciang, H. Dai, *Nat. Nanotechnol.* **2009**, *4*, 773.

[59] M. A. Lee, S. Wang, X. Jin, N. A. Bakh, F. T. Nguyen, J. Dong, K. S. Silmore, X. Gong, C. Pham, K. K. Jones, S. Muthupalani, G. Bisker, M. Son, M. S. Strano, *Adv. Healthc. Mater.* **2020**, *9*, 2000429.

[60] E. Hofferber, J. Meier, N. Herrera, J. Stapleton, C. Calkins, N. Iverson, *Nanomedicine Nanotechnology, Biol. Med.* **2022**, *40*, 102489.

[61] A. G. Beyene, K. Delevich, J. T. Del Bonis-O'Donnell, D. J. Piekarski, W. C. Lin,

A. Wren Thomas, S. J. Yang, P. Kosillo, D. Yang, G. S. Prounis, L. Wilbrecht, M. P. Landry, *Sci. Adv.* **2019**, *5*, eaaw3108.

[62] C. Bulumulla, A. T. Krasley, D. Walpita, A. G. Beyene, *bioRxiv* **2022**, 2022.01.19.476937.

[63] C. Paviolo, L. Cognet, *Neurobiol. Dis.* **2021**, *153*, 105328.

[64] D. A. Heller, R. M. Mayrhofer, S. Baik, Y. V Grinkova, M. L. Usrey, M. S. Strano, *J. Am. Chem. Soc.* **2004**, *126*, 14567.

[65] M. M. Safaee, M. Gravely, C. Rocchio, M. Simmeth, D. Roxbury, *ACS Appl. Mater. Interfaces* **2019**, *11*, 2225.

[66] A. Graf, Y. Zakharko, S. P. Schießl, C. Backes, M. Pfohl, B. S. Flavel, J. Zaumseil, *Carbon N. Y.* **2016**, *105*, 593.

[67] H. B, B. M, Z. X, *Annu. Rev. Biochem.* **2009**, *78*, 993.

[68] B. O. Leung, K. C. Chou, *Appl. Spectrosc.* **2011**, *65*, 967.

[69] X. Chen, Y. Wang, X. Zhang, C. Liu, *Biomater. Sci.* **2021**, *9*, 5484.

[70] G. H. Patterson, *Semin. Cell Dev. Biol.* **2009**, *20*, 886.

[71] V. E. lbbe, ao Professor in Jena, *Springer* **n.d.**

[72] Y. Yang, P. Wang, L. Lu, Y. Fan, C. Sun, L. Fan, C. Xu, A. M. El-Toni, M. Alhoshan, F. Zhang, *Anal. Chem.* **2018**, *90*, 7946.

[73] E. Hemmer, A. Benayas, F. Lé, F. Vetrone, *Nanoscale Horizons* **2016**, *1*, 168.

[74] C. Li, Q. Wang, *ACS Nano* **2018**, *12*, *10*, DOI 10.1021/acsnano.8b07536.

[75] K. Welsher, S. P. Sherlock, H. Dai, *Proc. Natl. Acad. Sci. U. S. A.* **2011**, *108*, 8943.

[76] J. Swoger, P. Verveer, K. Greger, J. Huisken, E. H. K. Stelzer, *Opt. Express* **2007**, *15*, 8029.

[77] F. Yang, Z. S. Deng, Q. H. Fan, *Micron* **2013**, *48*, 17.

[78] S. K. Maji, H. Yahia, *Sci. Rep.* **2019**, *9*, 1.

[79] W. H. Richardson, *J. Opt. Soc. Am.* **1972**, *62*, 55.

[80] L. B. Lucy, *Astron. J.* **1974**, *79*, 754.

[81] C. Belthangady, L. A. Royer, *Nat. Methods* **2019**, *16*, 1215.

[82] N. Gustafsson, S. Culley, G. Ashdown, D. M. Owen, P. M. Pereira, R. Henriques, *Nat. Commun. 2016 71* **2016**, *7*, 1.

[83] E. Nehme, L. E. Weiss, T. Michaeli, Y. Shechtman, *Optica* **2018**, *5*, 458.

[84] L. Schermelleh, A. Ferrand, T. Huser, C. Eggeling, M. Sauer, O. Biehlmaier, G. P. C. Drummen, *Cell Biol* **2019**, *21*, 72.

[85] M. Sauer, M. Heilemann, *Chem. Rev.* **2017**, *117*, 7478.

[86] N. Gustafsson, S. Culley, G. Ashdown, D. M. Owen, P. M. Pereira, R. Henriques, *Nat. Commun.* **2016**, *7*, 1.

[87] E. Betzig, G. H. Patterson, R. Sougrat, O. W. Lindwasser, S. Olenych, J. S. Bonifacino, M. W. Davidson, J. Lippincott-Schwartz, H. F. Hess, *Science* **2006**, *313*, 1642.

[88] S. T. Hess, T. P. K. Girirajan, M. D. Mason, *Biophys. J.* **2006**, *91*, 4258.

[89] M. J. Rust, M. Bates, X. Zhuang, *Nat Methods* **2006**, *3*, 793.

[90] M. Heilemann, S. Van De Linde, M. Schüttpelz, R. Kasper, B. Seefeldt, A. Mukherjee, P. Tinnefeld, M. Sauer, *Angew. Chemie - Int. Ed.* **2008**, *47*, 6172.

[91] A. Sharonov, R. M. Hochstrasser, *Proc. Natl. Acad. Sci. U. S. A.* **2006**, *103*, 18911.

[92] A. G. Godin, A. Setaro, M. Gandil, R. Haag, M. Adeli, S. Reich, L. Cognet, *Sci. Adv.* **2019**, *5*, eaax1166.

[93] M. Lelek, M. T. Gyparaki, G. Beliu, F. Schueder, J. Griffié, S. Manley, R. Jungmann, M. Sauer, M. Lakadamyali, C. Zimmer, *Nat. Rev. Methods Prim. 2021 11* **2021**, *1*, 1.

[94] M. A. A. Neil, R. Juškaitis, T. Wilson, *Opt. Lett.* **1997**, *22*, 1905.

[95] M. G. L. Gustafsson, *J. Microsc.* **2000**, *198*, 82.

[96] T. A. Klar, S. Jakobs, M. Dyba, A. Egner, S. W. Hell, *Proc. Natl. Acad. Sci. U. S. A.* **2000**, *97*, 8206.

[97] M. Hofmann, C. Eggeling, S. Jakobs, S. W. Hell, *Proc. Natl. Acad. Sci. U. S. A.* **2005**, *102*, 17565.

[98] T. Dertinger, R. Colyera, G. Iyer, S. Weiss, J. Enderlein, *Proc. Natl. Acad. Sci. U. S. A.* **2009**, *106*, 22287.

[99] S. Culley, K. L. Tosheva, P. Matos Pereira, R. Henriques, *Int J Biochem Cell Biol.* **2018**, *101*, 74.

[100] S. Elizarova, A. A. Chouaib, A. Shaib, B. Hill, F. Mann, N. Brose, S. Kruss, J. A. Daniel, *Proc. Natl. Acad. Sci.* **2022**, *119*, 1.

[101] H. Shen, L. J. Tauzin, R. Baiyasi, W. Wang, N. Moringo, B. Shuang, C. F. Landes, *Chem. Rev.* **2017**, *117*, 7331.

[102] C. A. Werley, W. E. Moerner, *J. Phys. Chem. B* **2006**, *110*, 18939.

[103] M. B. J. Roeffaers, B. F. Sels, H. Uji-i, F. C. De Schryver, P. A. Jacobs, D. E. De Vos, J. Hofkens, *Nature* **2006**, *439*, 572.

[104] N. Fakhri, A. D. Wessel, C. Willms, M. Pasquali, D. R. Klopfenstein, F. C. MacKintosh, C. F. Schmidt, *Science* **2014**, *344*, 1031.

[105] C. Paviolo, F. N. Soria, J. S. Ferreira, A. Lee, L. Groc, E. Bezard, L. Cognet, *Methods* **2020**, *174*, 91.

[106] K. I. Mortensen, L. S. Churchman, J. A. Spudich, H. Flyvbjerg, *Nat. Methods* **2010**, *7*, 377.

[107] A. Lee, K. Tsekouras, C. Calderon, C. Bustamante, S. Pressé, *Chem. Rev.* **2017**, *117*, 7276.

[108] R. Ehrlich, V. Wulf, A. Hendler-Neumark, B. Kagan, G. Bisker, *Opt. Express* **2022**,

30, 1130.

[109] T. Huokko, T. Ni, G. F. Dykes, D. M. Simpson, P. Brownridge, F. D. Conradi, R. J. Beynon, P. J. Nixon, C. W. Mullineaux, P. Zhang, L. N. Liu, *Nat Commun* **2021**, *12*, 1.

[110] J. A. Castillo-Badillo, A. C. Bandi, S. Harlalka, N. Gautam, *ACS Synth. Biol.* **2020**, *9*, 902.

[111] J. Sankaran, H. Balasubramanian, W. H. Tang, X. W. Ng, A. Röllin, T. Wohland, *Nat. Commun.* **2021**, *12*, 1.

[112] M. Venkatachalapathy, V. Belapurkar, M. Jose, A. Gautier, D. Nair, *Nanoscale* **2019**, *11*, 3626.

[113] G. Dey, S. Culley, S. Curran, U. Schmidt, R. Henriques, W. Kukulski, B. Baum, *Nature* **2020**, *585*, 119.

[114] H. Higuchi, S. Lee, H. Higuchi, *Biomed. Opt. Express* **2019**, *10*, 6611.

[115] S. Jin, N. Cordes, *Cell Commun. Signal.* **2019**, *17*, 1.

[116] F. Weihs, K. Wacnik, R. D. Turner, S. Culley, R. Henriques, S. J. Foster, *Sci Rep* **2018**, *8*, 1.

[117] Y. Han, X. Lu, Z. Zhang, W. Liu, Y. Chen, X. U. Liu, X. Hao, C. Kuang, X. U. Liu, X. Hao, X. Hao, C. Kuang, C. Kuang, C. Kuang, C. Kuang, A. C. Kuang, C. Kuang, *Opt. Express* **2019**, *27*, 38337.

[118] Y.-H. Lee, S. Zhang, C. K. Mitchell, Y.-P. Lin, J. O'brien, B. B. Author, *Biosci. Bioeng. (Boston, Mass.)* **2018**, *4*, 78.

[119] J. J. Zhang, N. Li, F. Dong, S. Liang, D. Wang, J. An, Y. Long, Y. Wang, Y. Luo, J. J. Zhang, *J. Ultrasound Med.* **2020**, *39*, 1507.

[120] A. Stubb, R. F. Laine, M. Miihkinen, H. Hamidi, C. Guzmán, R. Henriques, G. Jacquemet, J. Ivaska, *Nano Lett.* **2020**, *20*, 2230.

[121] P. Kelich, S. Jeong, N. Navarro, J. Adams, X. Sun, H. Zhao, M. P. Landry, L. V. Vuković*, *ACS Nano* **2022**, *16*, 736.

[122] J. M. Newby, A. M. Schaefer, P. T. Lee, M. G. Forest, S. K. Lai, *Proc. Natl. Acad. Sci. U. S. A.* **2018**, *115*, 9026.

[123] X. Gong, N. Renegar, R. Levi, M. Strano, *Machine Learning for the Discovery of Molecular Recognition Based on Single-Walled Carbon Nanotube Corona-Phases*, **2021**.

[124] V. Mannam, Y. Zhang, X. Yuan, C. Ravasio, S. S. Howard, *JPhys Photonics* **2020**, *2*, DOI 10.1088/2515-7647/abac1a.

[125] A. Durand, T. Wiesner, M. A. Gardner, L. É. Robitaille, A. Bilodeau, C. Gagné, P. De Koninck, F. Lavoie-Cardinal, *Nat. Commun.* **2018**, *9*, DOI 10.1038/S41467-018-07668-Y.

[126] Z. Liu, L. Jin, J. Chen, Q. Fang, S. Ablameyko, Z. Yin, Y. Xu, *Comput. Biol. Med.* **2021**, *134*, DOI 10.1016/J.COMPBIOMED.2021.104523.

[127] C. Ledig, L. Theis, F. Huszar, J. Caballero, A. Cunningham, A. Acosta, A. Aitken, A. Tejani, J. Totz, Z. Wang, W. Shi, *IEEE Conf. Comput. Vis. Pattern Recognit.* **2017**, 105.

[128] H. Zhao, Z. Ke, N. Chen, S. Wang, K. Li, L. Wang, X. Gong, W. Zheng, L. Song, Z. Liu, D. Liang, C. Liu, *J. Biophotonics* **2020**, *13*, e201960147.

[129] E. Nehme, B. Ferdman, L. E. Weiss, T. Naor, D. Freedman, T. Michaeli, Y. Shechtman, *IEEE Trans. Pattern Anal. Mach. Intell.* **2021**, *43*, 2179.

[130] Y. Wu, Y. Rivenson, H. Wang, Y. Luo, E. Ben-David, L. A. Bentolila, C. Pritz, A. Ozcan, *Nat. Methods* **2019**, *16*, 1323.

[131] A. Zaritsky, A. R. Jamieson, E. S. Welf, A. Nevarez, J. Cillay, U. Eskiocak, B. L. Cantarel, G. Danuser, *Cell Syst.* **2021**, *12*, 733.

[132] B. Lim, S. Son, H. Kim, S. Nah, K. M. Lee, in *IEEE Comput. Soc. Conf. Comput. Vis. Pattern Recognit. Work.*, **2017**, pp. 1132–1140.

[133] J. Zhang, T. Xu, X. Li, Y. Zhang, Y. Chen, X. Wang, S. Wang, C. Wang, *IEEE Photonics J.* **2020**, *12*, 6900914.

[134] C. Dong, C. C. Loy, K. He, X. Tang, *IEEE Trans. Pattern Anal. Mach. Intell.* **2016**, *38*, 295.

[135] J. Kim, J. K. Lee, K. M. Lee, in *CVPR*, **2016**.

[136] X. J. Mao, C. Shen, Y. Bin Yang, in *Adv. Neural Inf. Process. Syst.*, **2016**, pp. 2810–2818.

[137] Y. Rivenson, Z. Göröcs, H. Günaydin, Y. Zhang, H. Wang, A. Ozcan, *Optica* **2017**, *4*, 1437.

[138] J. Long, E. Shelhamer, T. Darrell, J. Long, T. Darrell, *Fully Convolutional Networks for Semantic Segmentation*, **2017**.

[139] O. Ronneberger, P. Fischer, T. Brox, *Lect. Notes Comput. Sci. (including Subser. Lect. Notes Artif. Intell. Lect. Notes Bioinformatics)* **2015**, *9351*, 234.

[140] Y. Lecun, L. Eon Bottou, Y. Bengio, P. H. Abstract|, *Proc. IEEE* **1998**, *86*, 2278.

[141] N. I. Chervyakov, P. A. Lyakhov, M. V. Valueva, *Proc. - 2017 Int. Multi-Conference Eng. Comput. Inf. Sci. Sib. 2017* **2017**, 135.

[142] M. V. Valueva, N. N. Nagornov, P. A. Lyakhov, G. V. Valuev, N. I. Chervyakov, *Math. Comput. Simul.* **2020**, *177*, 232.

[143] M. ’ A. Ranzato, F.-J. Huang, Y.-L. Boureau, Y. Lecun, in *IEEE Conf. Comput. Vis. Pattern Recognit.*, **2007**, pp. 1–8.

[144] W. Weng, X. Zhu, *IEEE Access* **2021**, *9*, 16591.

[145] A. K. Ray, *Information Technology : Principles and Applications*, Prentice-Hall Of India, **2004**.

[146] The MathWorks Inc., **2010**.

[147] S. R. S. R. Sternberg, *Computer (Long. Beach. Calif).* **1983**, *16*, 22.

[148] N. Otsu, *IEEE Trans Syst Man Cybern* **1979**, *SMC-9*, 62.

[149] A. L. Maas, A. Y. Hannun, A. Y. Ng, *Rectifier Nonlinearities Improve Neural Network Acoustic Models*, **2013**.

[150] K. He, X. Zhang, S. Ren, J. Sun, in *Comput. Vis. Pattern Recognit.*, **2016**, pp. 770–778.

[151] K. He, X. Zhang, S. Ren, J. Sun, in *Eur. Conf. Comput. Vis.*, **2016**, pp. 630–645.

[152] F. . & others. Chollet, **2015**.

[153] M. Abadi, A. Agarwal, P. Barham, E. Brevdo, Z. Chen, C. Citro, G. S. Corrado, A. Davis, J. Dean, M. Devin, S. Ghemawat, I. Goodfellow, A. Harp, G. Irving, M. Isard, Y. Jia, R. Jozefowicz, L. Kaiser, M. Kudlur, J. Levenberg, D. Mané, R. Monga, S. Moore, D. Murray, C. Olah, M. Schuster, J. Shlens, B. Steiner, I. Sutskever, K. Talwar, P. Tucker, V. Vanhoucke, V. Vasudevan, F. Viégas, O. Vinyals, P. Warden, M. Wattenberg, M. Wicke, Y. Yu, X. Zheng, G. Research, **2015**.

[154] S. Ioffe, C. Szegedy, *PMLR* **2015**, *37*.

[155] P. N. Stuart J. Russell, *Artificial Intelligence: A Modern Approach*, Prentice Hall ISBN, **2010**.

[156] D. P. Kingma, J. L. Ba, in *3rd Int. Conf. Learn. Represent. ICLR 2015 - Conf. Track Proc.*, International Conference On Learning Representations, ICLR, **2015**.

[157] L. N. Smith, in *IEEE Winter Conf. Appl. Comput. Vis.*, IEEE, **2017**.

[158] K. He, X. Zhang, S. Ren, J. Sun, in *ICCV*, **2015**.

[159] C.-Y. Yang, C. Ma, M.-H. Yang, *Comput. Vis. – ECCV* **2014**, *8692*.

[160] Z. Wang, A. C. Bovik, H. Rahim Sheikh, E. P. Simoncelli, *IEEE Trans. IMAGE*

Process. **2004**, *13*, DOI 10.1109/TIP.2003.819861.

[161] Z. Wang', Simoncelli', A. C. Bovik2, in *Thrity-Seventh Asilomar Conf. Signals, Syst. Comput.*, **2003**.

[162] P. Gupta, P. Srivastava, S. Bhardwaj, V. Bhateja, A Modified PSNR Metric Based on HVS for Quality Assessment of Color Images, **2011**.

Appendices

Table A1. Fine grid search results

combination	Epoch number	Batch size	Drop-out coefficient	L_1 penalizer weight λ	PSNR train set value	PSNR validation set value
52	100	8	0	0.25	38.568	37.762
1	50	8	0	0.1	38.048	37.948
27	75	8	0	0.25	38.269	37.770
28	75	8	0	0.5	38.250	37.729
53	100	8	0	0.5	38.375	37.724
29	75	8	0	0.75	37.925	37.565
26	75	8	0	0.1	37.103	37.070
31	75	8	0.05	0.1	36.967	36.960
30	75	8	0	1	37.686	37.224
7	50	8	0.05	0.25	36.961	37.313
6	50	8	0.05	0.1	36.908	37.272
3	50	8	0	0.5	37.399	37.374
32	75	8	0.05	0.25	36.810	36.876
5	50	8	0	1	37.493	37.624
56	100	8	0.05	0.1	36.708	36.685
55	100	8	0	1	37.504	37.135
8	50	8	0.05	0.5	36.725	37.121
4	50	8	0	0.75	37.079	37.191
9	50	8	0.05	0.75	36.675	37.041
57	100	8	0.05	0.25	36.595	36.508
11	50	8	0.1	0.1	36.269	36.669
33	75	8	0.05	0.5	36.665	36.202
34	75	8	0.05	0.75	36.360	36.097
58	100	8	0.05	0.5	36.282	36.165
35	75	8	0.05	1	36.149	35.999
36	75	8	0.1	0.1	35.717	35.523
14	50	8	0.1	0.75	35.894	36.281
59	100	8	0.05	0.75	35.861	35.653
17	50	8	0.15	0.25	35.350	35.882

37	75	8	0.1	0.25	35.211	35.095
16	50	8	0.15	0.1	35.178	35.763
38	75	8	0.1	0.5	35.142	35.124
18	50	8	0.15	0.5	35.073	35.556
39	75	8	0.1	0.75	35.254	35.306
42	75	8	0.15	0.25	35.062	35.249
41	75	8	0.15	0.1	35.020	35.239
40	75	8	0.1	1	35.238	35.220
19	50	8	0.15	0.75	35.078	35.502
43	75	8	0.15	0.5	34.838	34.963
45	75	8	0.15	1	34.886	34.939
21	50	8	0.2	0.1	34.984	35.572
47	75	8	0.2	0.25	34.589	34.677
44	75	8	0.15	0.75	34.629	34.677
12	50	8	0.1	0.25	34.977	35.140
2	50	8	0	0.25	34.990	35.166
61	100	8	0.1	0.1	35.111	34.871
20	50	8	0.15	1	34.946	35.299
46	75	8	0.2	0.1	34.451	34.406
49	75	8	0.2	0.75	34.450	34.415
48	75	8	0.2	0.5	34.471	34.425
50	75	8	0.2	1	34.485	34.441
15	50	8	0.1	1	35.219	35.456
23	50	8	0.2	0.5	35.038	35.292
24	50	8	0.2	0.75	35.135	35.279
22	50	8	0.2	0.25	34.749	35.075
62	100	8	0.1	0.25	35.131	34.869
10	50	8	0.05	1	34.655	34.996
25	50	8	0.2	1	34.626	34.943
13	50	8	0.1	0.5	34.460	34.796
54	100	8	0	0.75	35.173	34.656
63	100	8	0.1	0.5	35.201	34.795
65	100	8	0.1	1	35.149	34.641
67	100	8	0.15	0.25	34.863	34.217
60	100	8	0.05	1	34.457	33.975
64	100	8	0.1	0.75	34.457	33.981

68	100	8	0.15	0.5	34.477	34.010
66	100	8	0.15	0.1	34.488	34.015
72	100	8	0.2	0.25	34.524	34.055
71	100	8	0.2	0.1	34.568	34.101
69	100	8	0.15	0.75	34.580	34.113
70	100	8	0.15	1	34.584	34.118
74	100	8	0.2	0.75	34.617	34.154
75	100	8	0.2	1	34.653	34.195
73	100	8	0.2	0.5	34.681	34.220

תקציר

ננו-צינוריות פחמן חד-שכבתיות הינן בעלות תכונות אופטיות, כימיקליות ופיזיקליות ייחודיות, ובעלי יחס שטח פנים-לנפח גבוה, כאשר קוטרן הממוצע נע בין 1-2 ננומטר ואורכן יכול להגיע עד למספר מיקרומטרים. ננו צינוריות אלו יכולות לשמש ליישומי הדמיה וחישה ביו-רפואיים רבים, בייחוד בשל הקרינה הנפלטת האופיינית להן בטווח האינפרא-אדום הקרוב (בין 900 - 1400 ננומטר), החופף לטווח "חלון השקיפות הביולוגי". עם זאת, ומעבר לטבע הננומטרי שלהם שקטן מגודל הרזולוציה של המצלמה הנפוצה (0.7-13 מיקרומטר), בשל מגבלת העקיפה התלויה באורכי הגל, רזולוציית התמונות של ננו צינוריות תהיה נמוכה יותר ביחס לפלאורופורים סטנדרטיים, שכן אורכי הגל הנפלטים מננו הצינוריות ארוכים יותר בהשוואה לאלו הנפלטים מפלואורופורים הפולטים אורכי גל בטווח הנראה. לפיכך, טכניקות סופר-רזולוצייה אשר מאפשרות הבנה עמוקה ומדויקת יותר של תכונות מבניות-מרחביות והתנהגויות דינמיות בקנה מידה ננומטרי, נחוצות על מנת לנצל באופן מלא את פוטנציאל הננו צינוריות חד-שכבתיות כסמנים ביולוגיים ולחלץ בעזרתן כמה שיותר מידע מרחבי וזמני על סביבות ביולוגיות שונות. אף על פי כן, יישום של טכניקות סופר-רזולוציה על תמונות פלואורסצנטית של ננו-ציונוריות פחמן חד שכבתיות בטווח האינפרא-אדום הקרוב מעלה מספר אתגרים. ראשית, ננו-ציונוריות אלו אינן חלקיקים בעלות מבנה נקודתי, וייתכן שיתאפיינו בסיבובים, פיתולים ולולאות, דבר המונע הסתמכות על טכניקות סופר-רזולוציה מבוססות הנחות וחישובים גיאומטריים. יתרה מכך, ננו-צינוריות הפחמן הן הטרוגניות מטבען, כלומר בעלות התפלגות אורך רחבה ומגוון כיראליות רב, כשכל כריאליות משפיעה על אורך הגל הנפלט מהצינורית. לבסוף, אורכי הגל הארוכים יותר של הקרינה הנפלטת מהחלקיקים, בהשוואה לפלואורפורים נפוצים בטווח הנראה, מגבילים עוד יותר את הרזולוציה עקב מחסום העקיפה.

עבודה זו מדגימה את השימוש בלמידה עמוקה באופן כללי, וברשתות קונבולוציה בפרט, להשגת תמונות ברזולוציה גבוהה של ננו צינוריות פחמן חד-שכבתיות בטווח הספקטרלי של האינפרא-אדום הקרוב. תוך ניצול היתרונות של למידה עמוקה ורשתות קונבולוציה, הצלחנו לייצר תמונות ברזולוציה גבוהה עבור טווח רחב של צפיפויות ואורכים של ננו צינוריות בתמיסות המצולמות, וכמו כן גם עבור מגוון רחב של תנאי הדמיה עם יחסי אות-לרעש מאתגרים. עבודה זו מציגה, לראשונה, גישת סופר-רזולוציה רובסטית שאינה דורשת כוונון פרמטרים ידני או ציוד אופטי מיוחד.

יתרה מכך, הגישה שלנו אינה מצריכה פלואורפורים סטוכסטיים או מהבהבים, בניגוד לשיטות סופר-רזולוציה אחרות כגון שחזור אופטי של מיקרוסקופיה סטוכסטית (**STORM**) או לוקליזציה פוטו-פעילה (**PALM**).

בעבודה זו, אימנו רשת קונבולוציה בעל ארכיטקטורת "צוואר-בקבוק", המבוססת על עקרון קידוד ופענוח, תוך למידה מונחה על בסיס שיטה אנליטית קיימת לסופר-רזולוציה, הנקראת תנודות רדיאליות ברזולוצית-על (**SRRF**). בחנו את הרשת שלנו על תמונות חדשות ונוכחנו לגלות שיפור בולט הן ברזולוציה והן ביחס האות-רעש עבור מגוון רחב של צורות, אורכים וצפיפויות שונות של ננו צינוריות הפחמן. יתרה מכך, הדגמנו יישום של סופר-רזולוציה בשיטה זו בזמן אמת על סרטונים המתעדים תנודות של ננו-הצינוריות, מבלי להתפשר על הרזולוציה הזמנית של רצף הפריימים המקורי. עבודה זו מספקת אבן דרך משמעותית בתחום המיקרוסקופיה ברזולוציית-על תוך שימוש בטכניקות למידה עמוקה להשגת אלגוריתם מהיר במיוחד, ללא פרמטרים, ליצירת תמונות סופר-רזולוציה בטווח האינפרא-אדום הקרוב, של חלקיקים שאינם כדוריים ככלל, ושל ננו-צינוריות פחמן חד שכבתיות בפרט, דבר היוכל לקדם אותנו צעד נוסף לעבר שימוש מעשי בצינוריות כסמנים אופטיים-ביולוגיים בקנה המידה ננומטרי.

אוניברסיטת תל - אביב
הפקולטה להנדסה ע"ש איבי ואלדר פליישמן
בית הספר לתארים מתקדמים ע"ש זנדמן-סליינר

סופר-רזולוציה של ננו-צינוריות פחמן חד-שכבתיות הפולטות פלורסנציה באינפרא-אדום הקרוב

חיבור זה הוגש כעבודת גמר לקראת התואר "מוסמך אוניברסיטה" בהנדסה ביו-רפואית

על-ידי

ברק כגן

העבודה נעשתה במחלקה להנדסה ביו-רפואית

בהנחית ד"ר גילי ביסקר
תשרי תשפ"ג

אוניברסיטת תל - אביב
הפקולטה להנדסה ע"ש איבי ואלדר פליישמן
בית הספר לתארים מתקדמים ע"ש זנדמן-סליינר

סופר-רזולוציה של ננו-צינוריות פחמן חד-שכבתיות הפולטות פלורסנציה באינפרא-אדום הקרוב

חיבור זה הוגש כעבודת גמר לקראת התואר "מוסמך אוניברסיטה" בהנדסה ביו-רפואית

על-ידי

ברק כגן

תשרי תשפ"ג